

# Distant clusters of galaxies in the 2XMM/SDSS footprint: follow-up observations with the LBT<sup>★,★★,★★★</sup>

A. Rabitz<sup>1</sup>, G. Lamer<sup>1</sup>, A. Schwobe<sup>1</sup>, and A. Takey<sup>2</sup>

<sup>1</sup> Leibniz-Institut für Astrophysik Potsdam (AIP), An der Sternwarte 16, 14482 Potsdam, Germany  
e-mail: arabitz@aip.de

<sup>2</sup> National Research Institute of Astronomy and Geophysics (NRIAG), 11421 Helwan, Cairo, Egypt

Received 8 May 2017 / Accepted 11 July 2017

## ABSTRACT

**Context.** Galaxy clusters at high redshift are important to test cosmological models and models for the growth of structure. They are difficult to find in wide-angle optical surveys, however, leaving dedicated follow-up of X-ray selected candidates as one promising identification route.

**Aims.** We aim to increase the number of galaxy clusters beyond the SDSS-limit,  $z \sim 0.75$ .

**Methods.** We compiled a list of extended X-ray sources from the 2XMMp catalogue within the footprint of the Sloan Digital Sky Survey. Fields without optical counterpart were selected for further investigation. Deep optical imaging and follow-up spectroscopy were obtained with the Large Binocular Telescope, Arizona (LBT), of those candidates not known to the literature.

**Results.** From initially 19 candidates, selected by visually screening X-ray images of 478 *XMM-Newton* observations and the corresponding SDSS images, 6 clusters were found in the literature. Imaging data through  $r, z$  filters were obtained for the remaining candidates, and 7 were chosen for multi-object (MOS) spectroscopy. Spectroscopic redshifts, optical magnitudes, and X-ray parameters (flux, temperature, and luminosity) are presented for the clusters with spectroscopic redshifts. The distant clusters studied here constitute one additional redshift bin for studies of the  $L_X - T$  relation, which does not seem to evolve from high to low redshifts.

**Conclusions.** The selection method of distant galaxy clusters presented here was highly successful. It is based solely on archival optical (SDSS) and X-ray (*XMM-Newton*) data. Out of 19 selected candidates, 6 of the 7 candidates selected for spectroscopic follow-up were verified as distant clusters, a further candidate is most likely a group of galaxies at  $z \sim 1.21$ . Out of the remaining 12 candidates, 6 were known previously as galaxy clusters, one object is a likely X-ray emission from an AGN radio jet, and for 5 we see no clear evidence for them to be high-redshift galaxy clusters.

**Key words.** galaxies: clusters: general – galaxies: clusters: intracluster medium – X-rays: galaxies: clusters – cosmology: observations

## 1. Introduction

Clusters of galaxies are considered the largest gravitationally bound structures in the Universe, and they emit radiation on a wide wavelength range. The multi-component nature of clusters gives rise to various detection methods, since distinct physical effects contribute to different parts of the spectrum they emit. Beneath the main component of galaxy clusters, which is thought to be composed of dark matter and is hence not directly observable, the next major fraction is the hot ionized intra-cluster medium

(ICM). The ICM can be observed through thermal emission of its gravitationally heated gas, which mainly emits in the soft X-ray regime. Inverse-Compton scattering of the ICM and photons of the cosmic microwave background, the Sunyaev-Zel'dovich (SZ) effect; Sunyaev & Zeldovich 1972), can be investigated at millimeter wavelengths. Optical and near-infrared (near-IR) observations, however, allow redshift measurements with moderate effort, and for instance reveal the dynamical state of the galaxy population of the cluster, as well as the morphology and star formation history of the individual members. The suitability of different wavelength regimes for detecting galaxy clusters is proven by various campaigns, for example Böhringer et al. (2001), Gladders & Yee (2005), and Vale & White (2006) for the selection using X-ray, optical, and millimeter wavelength, respectively.

Important properties of galaxy clusters such as their number density and masses deliver important constraints for cosmological models. Large-area X-ray surveys like the ROSAT All Sky Survey (Voges et al. 1999) detected large numbers of clusters, see for example the Meta-Catalog of X-ray detected Clusters of galaxies (MCXC; Piffaretti et al. 2011). Observations with *XMM-Newton* increase the number of deeply exposed regions of the X-ray sky, allowing for different luminosity constraints of potential clusters. Many cluster surveys are based on X-ray

\* Based on observations obtained with *XMM-Newton*, an ESA science mission with instruments and contributions directly funded by ESA Member States and NASA.

\*\* The LBT is an international collaboration among institutions in the United States, Italy and Germany. LBT Corporation partners are: the University of Arizona on behalf of the Arizona Board of Regents; Istituto Nazionale di Astrofisica, Italy; LBT Beteiligungsgesellschaft, Germany, representing the Max-Planck Society, The Leibniz Institute for Astrophysics Potsdam, and Heidelberg University; The Ohio State University, and The Research Corporation, on behalf of The University of Notre Dame, University of Minnesota and University of Virginia – <http://www.lbto.org/for-investigators.html>

\*\*\* The catalogue, similar to Table A.1, is also available at the CDS via anonymous ftp to [cdsarc.u-strasbg.fr](http://cdsarc.u-strasbg.fr) (130.79.128.5) or via <http://cdsarc.u-strasbg.fr/viz-bin/qcat?J/A+A/607/A56>

selection and optical verification of sources, either working on complete sets of archival data for the lower redshift regime (e.g. *XMM-Newton* and SDSS; Takey et al. 2011, 2013, 2016) or on fields that require dedicated deep follow-up imaging and spectroscopy for discovering low-luminosity and high-redshift clusters (e.g. Fassbender et al. 2011; Pacaud et al. 2016).

Large samples of clusters were confirmed using the redsequence method from photometric data of optical sky surveys, for example the MaxBCG Catalog based on SDSS photometry (Koester et al. 2007) and redMaPPer using data from SDSS and the Dark Energy Survey (DES; Rykoff et al. 2016). Other cluster surveys make use of spectroscopically confirmed galaxies as verification, for instance spectra of BCGs from the SDSS (Takey et al. 2011). However, redshifts from SDSS data alone (either photometric or spectroscopic) are limited to redshifts below  $z \sim 0.75$ . Buddendiek et al. (2015) cross-matched ROSAT All Sky Surveys sources with red galaxies from the SDSS, and using follow-up observations with the *William Herschel* Telescope (WHT) and the Large Binocular Telescope, Arizona (LBT), they were able to identify clusters at  $0.6 \lesssim z \lesssim 1.0$ . Bleem et al. (2015) conducted a study using the SZ effect to discover galaxy clusters. Since the dimming of the observed SZ flux caused by the luminosity distance to the cluster is partly compensated for by the higher energy density of the cosmic microwave background (CMB) at higher redshifts, current SZ surveys (e.g. from the SPT) allow probing high-mass galaxy clusters out to  $z > 1$ . Bleem et al. (2015) used IR imaging and spectroscopy of *Spitzer* and ground-based facilities to verify overdensities of galaxies and to determine their redshift. Another approach is to select clusters purely on their near-IR and IR colour, where the  $z$ -band and the  $3.6 \mu\text{m}$  band of *Spitzer*, for instance, allow for tracing the  $4000 \text{ \AA}$  break of galaxies out to  $z > 1$  (e.g. Muzzin et al. 2009; Webb et al. 2015; Wilson et al. 2009).

Here we investigate galaxy clusters that were serendipitously found by *XMM-Newton* observations and are listed in the 2XMMp catalogue, the predecessor of the public 2XMM catalogue (Watson et al. 2009). By explicitly considering SDSS blank fields in our selection, we intend to increase the number of high-redshift ( $z \sim 1$ ) galaxy clusters. This is the redshift regime where existing large-area optical surveys lack sensitivity to unambiguously confirm these clusters. We carried out follow-up observations at the LBT using the LBC prime focus camera for imaging and MODS for multi-object spectroscopy, resulting in identifications of six new clusters and one high-redshift group. Furthermore, six of the selected X-ray sources were identified with clusters of galaxies that have been published previously.

This new sample complements the cluster samples published by Takey et al. (2013) and Takey et al. (2014), which were also selected from the 2XMM catalogue, adding 13 high-redshift objects to the cluster identifications in the 2XMM/SDSS footprint.

The paper is organized as follows: in Sect. 2 we explain the sample definition based on archival *XMM-Newton* data. Details on data reduction and the analysis of optical pre-imaging and spectroscopic follow-up are outlined in Sects. 3 and 4, respectively. The treatment of archival X-ray data is described in Sect. 5. Section 6 presents the results of this work. We describe how we derive the spectroscopic properties and cluster mass (Sect. 6.1), the generation and treatment of X-ray spectra to measure fluxes and ICM temperatures (Sect. 6.2), and detail the properties of the individual clusters in the following subsections. An analysis of the  $L-T$  relation (Sect. 6.6), using our sample in comparison to data from the literature, concludes the results section. We summarize our findings in Sect. 7. In Appendix we list photometric and spectroscopic properties of the fields

observed with LBC and MODS at the LBT (Appendix A), and present optical and IR images of the previously known clusters (Appendix B), as well as of the rejected or unclassified fields (Appendix C).

Throughout the paper we assume a standard cosmology with  $\Omega_M = 0.3$ ,  $\Omega_\Lambda = 0.7$  and  $H_0 = 70 \text{ km s}^{-1} \text{ Mpc}^{-1}$ . The critical density of the Universe for the respective mean cluster redshifts can be derived using  $\rho_c = 3H(z)^2 \cdot (8\pi \text{ G})^{-1}$ , with the gravitational constant  $G$  and the Hubble parameter  $H(z)$ . All given optical magnitudes refer to the AB system.

## 2. Sample definition

The catalogue 2XMMp, a pre-release of the second *XMM-Newton* catalogue (2XMM; Watson et al. 2009), lists all sources detected with the XMM-EPIC cameras in  $\sim 2400$  observations before April 2006, covering an area on the sky of  $\sim 360 \text{ deg}^2$ . When this project started, the 2XMMp catalogue was the current and most complete catalogue of *XMM-Newton* serendipitous sources. Since then, the *XMM-Newton* catalogue was updated continuously through incremented observations and changes in the data reduction pipeline. In Sect. 5 we compare the initial sample parameters to the more recent 3XMM-DR6 catalogue (Rosen et al. 2016).

For our cluster sample we selected only observations within the footprint of the Sloan Digital Sky Survey DR6 (Adelman-McCarthy et al. 2008) and at Galactic latitudes  $|b_{II}| > 20^\circ$ . Observations not suitable for the detection of extended sources (e.g. because of very extended or very bright targets, or observations with severe background contamination) were removed by means of visual screening of the EPIC images. This reduced the number of EPIC pointings used for the compilation of our input catalogue to 478. When we take repeated or overlapping pointings in the same sky area into account, the total survey area is  $\sim 60 \text{ deg}^2$ .

For the 2XMM data processing, the source detection pipeline of XMM-SAS version 7.1 was used in a configuration enabling the classification of sources as point-like or extended. Extended sources were fitted with radially symmetric  $\beta$ -profiles, convolved with the corresponding EPIC point-spread function (PSF), in order to determine the source parameters. Since the spurious detection rate of extended sources is relatively high (e.g. near bright point-sources or because of blending of multiple point-sources), another visual screening step was necessary to clean the sample. The final list of extended sources comprises 412 entries.

In order to identify candidates for distant galaxy clusters, we correlated the source positions with the SDSS DR6 photometric and spectroscopic catalogues and generated SDSS finding charts for each of the extended X-ray sources. This correlation yielded 393 extended X-ray sources with either a galaxy or cluster candidate detected in the SDSS.

Only 19 sources of our selection (see Table 1) have no plausible counterpart in the SDSS imaging and therefore are considered as candidates for distant clusters of galaxies, where the member galaxies are beyond the detection limit of the SDSS.

## 3. Optical pre-imaging

### 3.1. Imaging data – data description and reduction

Deep optical imaging for 13 of the initial 19 fields was carried out between March 2008 and November 2011 at the LBT. Our imaging strategy included binocular observation to efficiently use the telescope capabilities. LBC-blue and LBC-red

**Table 1.** List of all X-ray selected galaxy cluster candidates within SDSS blank fields.

Name	RA(J2000)	Dec(J2000)	LBT/LBC	LBT/MODS	$z$	Ref.
2XMMp J030212.0-000133	03:02:12.1	-00:01:32	–	–	1.185	Šuhada et al. (2011)
2XMMp J083026.2+524133	08:30:26.2	+52:41:33	$r, z$ (0.3 h)	1.5 h	$0.9855 \pm 0.0037$	<i>this work</i>
2XMMp J084836.4+445345	08:48:36.1	+44:53:43	–	–	1.273	Stanford et al. (1997)
2XMMp J084858.3+445158	08:48:58.4	+44:51:58	–	–	1.261	Rosati et al. (1999)
2XMMp J092120.2+371735	09:21:20.2	+37:17:35	$r, z$ (0.6 h)	2.5 h	$1.2134 \pm 0.0014$	<i>this work</i>
2XMMp J093437.4+551340	09:34:37.5	+55:13:42	$r, z$ (0.48 h)	1.5 h	$0.83855 \pm 0.00094$	<i>this work</i>
2XMMp J093607.2+613245	09:36:07.3	+61:32:45	$r, z$ (0.73 h)	–	–	–
2XMMp J100451.6+411626	10:04:51.6	+41:16:27	–	–	0.82	Hoefl et al. (2008)
2XMMp J105320.0+440816	10:53:19.8	+44:08:17	$r, z$ (0.62 h)	2.0 h	$0.8955 \pm 0.0032$	<i>this work</i>
2XMMp J105344.2+573517	10:53:43.5	+57:35:18	$z$ (0.3 h)	–	1.134	Hashimoto et al. (2005)
2XMMp J120735.1+250538	12:07:35.2	+25:05:37	$r, z$ (0.3 h)	–	–	–
2XMMp J120815.5+250001	12:08:16.0	+25:00:02	$r, z$ (0.3 h)	2.0 h	$0.9912 \pm 0.0027$	<i>this work</i>
2XMMp J123113.1+154550	12:31:13.1	+15:45:48	–	–	0.893	Rabitz et al. (in prep.)
2XMMp J123759.3+180332	12:37:59.2	+18:03:35	$r, z$ (0.3 h)	2.0 h	$0.8874 \pm 0.0024$	<i>this work</i>
2XMMp J133038.6-013832	13:30:38.7	-01:38:32	$r, z$ (0.3 h)	–	–	–
2XMMp J133853.9+482033	13:38:54.1	+48:20:34	$r, z$ (0.85 h)	2.0 h	$0.7517 \pm 0.0016$	<i>this work</i>
2XMMp J144854.8+085400	14:48:54.7	+08:53:59	$r, z$ (0.3 h)	–	–	Lamer et al. (2011)
2XMMp J145220.8+165458	14:52:20.6	+16:54:57	$r, z$ (0.77 h)	–	–	–
2XMMp J151716.8+001302	15:17:16.9	+00:12:58	$r, z$ (0.3 h)	–	–	–

**Notes.** Summary of the observational state of our sample. The first column lists the extended X-ray emission in the 2XMMp catalogue, from which this sample is built. The coordinates based on a cross-correlation with the 3XMM-DR6 catalogue are given in Cols. 2 and 3. The next two columns state the exposure time spent at imaging in LBT/LBC  $r$ -SLOAN,  $z$ -SLOAN, and at spectroscopy with LBT/MODS, respectively, followed by the spectroscopic redshift (Col. 6) and its reference (Col. 7).

were equipped with  $r$ -SLOAN and  $z$ -SLOAN filters, respectively. Dither patterns of at least nine positions with single-exposure times of 90 s or 120 s were used to cleanly bridge the chip gaps of the instruments in the reduced images. For details on the individual target coordinates and the exposure times, we refer to Table 1.

All imaging data were reduced with the code THELI (Schirmer 2013; Erben et al. 2005). The reduction included subtracting a master-bias and flat-fielding the raw data using sky-flats, applying a background-model correction to reduce the imprinted fringing pattern, weighting, astrometric calibration, and coaddition of the individual science exposures. The photometric zero-point (AB system) of the mosaic image was calculated using the SDSS-DR9 catalogue data as reference.

We extracted AB magnitudes using SExtractor (Bertin & Arnouts 1996) with critical settings that affect background estimation and object detection fixed for all fields and filters. The dual-image mode of SExtractor was used to simultaneously measure isophotal object magnitudes in  $r$ -SLOAN and  $z$ -SLOAN images on fixed positions that were determined on the  $z$ -band images. The limiting magnitude of the coadded mosaics, taking the flux from the sky background within a given aperture into account, is given by

$$m_{\text{lim}} = ZP - 2.5 \log \left( 5 \sqrt{N_{\text{pix}}} \sigma_{\text{sky}} \right), \quad (1)$$

where we use the zero-point (ZP), the number of pixels ( $N_{\text{pix}}$ ) within the aperture with  $2''$  radius, and the variation of the sky background as measured by SExtractor. The resulting  $5\sigma$  detection limits for both filters are  $25.42 < r_{\text{lim}} < 26.49$  and  $24.41 < z_{\text{lim}} < 25.49$ , depending on the total exposure times of 0.3 to 0.85 hours.

False-colour images, created from the reduced  $r$ -SLOAN and  $z$ -SLOAN exposures, are shown in Sect. 6 and the respective sub-paragraphs for each of the seven spectroscopically confirmed galaxy clusters.

### 3.2. Target selection for spectroscopic follow-up

We inspected the colour–magnitude diagrams of all fields in order to select the tentative cluster galaxies using the red-sequence method (see Gladders & Yee 2000). In these colour–magnitude plots, the colour of passive galaxies shows a clear dependency on redshift, which is due to the prominence of the Balmer break (4000 Å at restframe). Hence, galaxies of the same cluster undergoing similar evolution will scatter little in colour, but vary in magnitude. Since the fraction of early-type cluster member galaxies decreases with redshift, the red sequence for distant clusters may be only sparsely populated. For this reason, not only the colour was decisive for the selection of a possible BCG and cluster galaxies, but also the position with respect to the extended X-ray emission and the actual observability, such as brightness and typical constraints of multi-object spectroscopy (slit collision and possible spectral overlap). Wherever possible, we filled the remaining space on the slit-masks with less likely targets and objects of opportunity (e.g. isolated X-ray sources or possible lensing features). Colour–magnitude diagrams of the six spectroscopically confirmed clusters are shown in Figs. 5 and 6.

## 4. Spectroscopic follow-up

### 4.1. Spectroscopy – data description

The spectroscopic follow-up was executed in February and March 2012. The instrument of choice for this campaign was the Multi-Object Double Spectrograph (MODS; Pogge et al. 2010) at the LBT. For each of the seven follow-up fields, one multi-slit mask (MOS-mask) was cut, intended to cover the most probable cluster galaxy candidates (see Sect. 3.2) and a few objects of opportunity. We only observed using the red spectral arm of MODS with grating G670L, resulting in a spectral coverage of 5200–10 000 Å. Depending on the target brightness and observing conditions, we took up to five individual exposures of

30 min per field; the total exposure time per field is summarized in Table 1.

#### 4.2. Spectroscopy – data reduction

Data reduction was performed as a two-stage process: pre-reduction, and pipeline reduction. During pre-reduction we made use of `modsCCDRed`<sup>1</sup>, a set of Python-scripts that subtracted the bias-pattern and applied a flat-field correction. The resulting pre-reduced data were further reduced with a set of scripts written mainly in ESO-Midas. These scripts were initially intended to reduce VLT/FORS2 data, but are perpetually generalised to suit different multi-object spectroscopy instruments, including MODS.

The workflow of the pipeline reduction includes the following tasks: cosmic filtering of scientific frames, wavelength calibration, weighted extraction of 1D spectra (following Horne 1986), including generation of respective error spectra, creation of 2D sky-subtracted frames, and co-addition of single spectra. Spectrophotometric standard stars observed during our observation period were used to flux-calibrate the final spectra.

#### 4.3. Spectroscopy – data analysis

We were able to extract a total of 215 spectra from our data. All 1D flux- and error-spectra were inspected with EZ (a tool for automatic redshift measurement, see Garilli et al. 2010) to obtain first impressions on quality and redshift of each individual spectrum. The first inspection revealed 194 preliminary redshifts, of which 176 were graded secure because they showed several spectral features. In these science-grade spectra, we identified 10 late-type stars. Spectra of obvious galaxy cluster candidates, primarily passive galaxies (see Sect. 3.2), were inspected in more detail. We measured their redshift by fitting a double-Gaussian to the prominent CaII H&K absorption lines, or alternatively, when the signal-to-noise ratio was found to be too low, by solely fitting the [OII] (3727 Å) emission. All galaxy redshifts were converted into the barycentre of the solar system. In Fig. 1 we show a histogram of all science-grade redshifts from our spectroscopic program, where the inset highlights the redshifts of the successfully identified clusters.

## 5. Archival X-ray data and data reduction

The whole sample of extended sources was initially selected from the 2XMMp (see Sect. 2). Since in the meantime the number of *XMM-Newton* observations (OBSIDs) and the knowledge on the instruments have vastly increased, we compared our initial targets with the recent 3XMM-DR6 catalogue (Rosen et al. 2016) to ensure that the detections are characterized as extended sources. For all initial targets, we found an extended detection in the 3XMM-DR6, with the exception of 2XMMp J145220.8+165458, which is now classified as a point source. The extents of all other sources agreed well and were mostly within the errors of the two catalogues. The number of observations covering our sample increased from 28 to 36 between 2XMMp and 3XMM-DR6. A comparison between 2XMMp and 3XMM-DR6, containing source-identifiers (SRCID), extent parameters (EP\_EXTENT), and OBSID, is listed in Table D.1. The table also contains the flare-cleaned

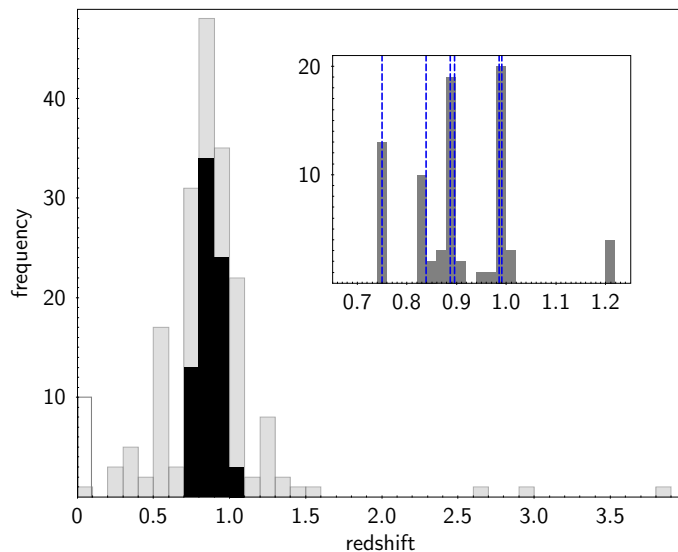


**Fig. 1.** Histogram built from all spectra of our spectroscopic observations. The transparent region in the main plot marks the content of stars identified in the sample, the light shaded regions reflect the content of galaxies, where the fraction of all identified cluster member galaxies is plotted black. The inset details the mean cluster redshift as vertical blue dashed lines overplotted on the histogram of the identified member galaxies that match our selection criteria.

exposure time for the EPIC instruments for all OBSIDs from which we extracted spectra (see Sect. 6.2).

We downloaded all publicly available *XMM-Newton* observations until December 2015 that overlapped our sample from the *XMM-Newton* Science Archive (XSA; Arviset et al. 2002). The data reduction and analysis was carried out using the *XMM-Newton* Science Analysis Software (SAS) version 15. From background-flare-cleaned event file lists, we generated X-ray images in the energy range between 0.5 and 3.0 keV for each EPIC camera and OBSIDs individually.

## 6. Results: galaxy and cluster properties

### 6.1. Cluster redshifts and dynamical masses

In this section we describe our procedure of cluster member selection and the velocity dispersion and dynamical mass calculation for the seven fields of which we have dedicated spectroscopic data from LBT/MODS. We proceed with the analysis of the *XMM-Newton* data, from which we extract spectra and compute fluxes, luminosities, and temperatures. We give the results and further details for all selected fields, which are grouped according to their available data and properties: (i) the six fields of newly confirmed clusters with LBT/MODS spectroscopy; (ii) targets with no spectroscopy from this work, but published redshifts from the literature; and (iii) the remaining fields containing a high-redshift group of galaxies, and candidates that are not yet confirmed or are rejected.

At this point, we also introduce images from the Wide-field Infrared Survey Explorer (WISE, see Wright et al. 2010), whose imaging bands are centred at 3.4, 4.6, 12, and 22  $\mu\text{m}$  (W1–W4). Especially the bands W1 and W2 are useful for colour-selecting galaxies between  $0.75 < z < 1.75$  because of an apparently monotonical reddening. This method was introduced by Papovich (2008) and later adopted by Gettings et al. (2012) for their search for distant galaxy clusters using WISE data. Cutout IR images from WISE for our cluster candidates therefore allow

<sup>1</sup> <http://www.astronomy.ohio-state.edu/MODS/Software/modsCCDRed/>

**Table 2.** Cluster properties from optical and X-ray spectroscopy.

Name	$n$	$z_{\text{cl}}$	$\sigma$	$r_{200}$	$M_{200}$	$F_{0.5-2}(300 \text{ kpc})$	$L_{\text{bol}}(r_{500})$	$k_{\text{B}}T$
2XMMp J083026.2+524133	8	0.9856(27)	$930^{+300}_{-230}$	$2.44^{+0.79}_{-0.6}$	$5.1^{+6.7}_{-2.9}$	$6.477 \pm 0.095$	$1168 \pm 4$	$7.82^{+0.4}_{-0.39}$
2XMMp J093437.4+551340	11	0.83858(73)	$430^{+120}_{-96}$	$1.24^{+0.35}_{-0.28}$	$0.56^{+0.62}_{-0.3}$	$7.4 \pm 0.83$	$56 \pm 6.1$	$2.96^{+0.86}_{-0.65}$
2XMMp J105319.8+440817	8	0.8955(32)	$780^{+660}_{-360}$	$2.14^{+1.82}_{-0.97}$	$3.1^{+16.6}_{-2.6}$	$2.37 \pm 0.27$	$240 \pm 25$	$3.6^{+1.2}_{-0.76}$
2XMMp J120815.5+250001	16	0.9929(26)	$1200^{+300}_{-240}$	$3.13^{+0.78}_{-0.62}$	$10.9^{+10.3}_{-5.3}$	$2.79 \pm 0.42$	$363 \pm 44$	$4.1^{+2.2}_{-1.1}$
2XMMp J123759.3+180332	16	0.8874(24)	$1200^{+310}_{-250}$	$3.31^{+0.87}_{-0.7}$	$11.4^{+11.6}_{-5.8}$	$4.75 \pm 0.47$	$536 \pm 40$	$5.0^{+1.9}_{-1.1}$
2XMMp J133853.9+482033	8	0.74969(30)	$122^{+32}_{-26}$	$0.37^{+0.1}_{-0.07}$	$0.013^{+0.014}_{-0.006}$	$1.1 \pm 0.16$	$148 \pm 22$	–

**Notes.** The dynamical mass  $M_{200}$  is given in  $10^{14} M_{\odot}$ ,  $r_{200}$  in Mpc. The errors of  $\sigma$  correspond to a confidence interval of 90%,  $M_{200}$  and  $r_{200}$  furthermore include the uncertainty in  $A_{\text{ID}}$ . The X-ray properties flux and ICM temperature are based on measurements within a radius of 300 kpc, the bolometric luminosity was extrapolated to  $r_{500}$  (details see Sect. 6.2). The X-ray flux is in units of  $10^{-14} \text{ erg cm}^{-2} \text{ s}^{-1}$ , the luminosity in  $10^{42} \text{ erg s}^{-1}$ . Note that two clusters (2XMMp J120815.5+250001 and 2XMMp J123759.3+180332) have extremely large dynamical mass estimates ( $>10^{15} M_{\odot}$ ) but, for this sample, an average ICM temperature. The dynamical mass estimates might be overestimated due to velocity measurements from galaxies not gravitationally bound to the cluster (see Sects. 6.3.4 and 6.3.5).

high-redshift galaxies to be better recognized than from optical survey data (SDSS) alone. We did not use the IR colour as an excluding criterion for the decision between low and high redshift of clusters – a qualitative examination of this criterion is part of ongoing work comprising a larger sample of galaxy clusters, and will be presented in a future paper (Rabitz et al., in prep.). As additional detail for the LBT/MODS confirmed clusters, we provide cutouts from the SDSS, WISE, and LBC pre-imaging of the respective cluster fields (Figs. 2–4) together with photometric and spectroscopic results from our observations (Figs. 5 and 6).

Since LBT imaging data are also available for groups (ii) and (iii) of our data, we present the respective LBC images and SDSS finding charts in Appendices B and C, while additional information for the high-redshift group of galaxies are given in Figs. 7–9.

We summarize the properties of the LBT/MODS-confirmed clusters in Table 2, and those of the clusters with references in Table 3. To evaluate cluster redshift and velocity dispersion, we adopted the bi-weight method outlined in Beers et al. (1990). Our strategy to determine  $z_{\text{cl}}$  was as follows. We selected all galaxies as preliminary cluster members fulfilling  $|z_{\text{mem}} - z_{\text{BCG}}| \cdot c \leq 4000 \text{ km s}^{-1}$ , where we used the redshift of an obvious brightest cluster galaxy  $z_{\text{BCG}}$  and the speed of light  $c$ , and calculated the preliminary cluster redshift and its velocity dispersion. Using a conservative clipping based on the preliminary velocity dispersion,  $|z_{\text{pre}} - z_{\text{mem}}| \cdot c \leq 3\sigma_{\text{pre}} \cdot (1 + z_{\text{pre}})$ , we rejected further galaxies from the sample in order to derive updated bi-weight estimators and repeated this step when necessary. Errors were calculated from  $10^5$  bootstrap simulations and the 90% confidence interval of jackknife rebinning, for  $z_{\text{cl}}$  and  $\sigma$ , respectively, as recommended in Beers et al. (1990).

For clusters with very few member galaxies, we were unable to calculate a statistically meaningful velocity dispersion. We therefore show the number of galaxies ( $n$ ) taken into account for the calculation in Table 2. All  $\sigma$  values were scaled to the cluster redshift (factorized with  $(1 + z_{\text{cl}})^{-1}$ , as stated in Peebles 1993).

Munari et al. (2013) examined the relation between the velocity dispersion of different physical tracers in simulated galaxy clusters to the mass of their respective dark matter halos, where they used Navarro-Frenk-White (NFW; Navarro et al. 1997) profile fits. We averaged the best-fitting parameters they found for

the two corresponding simulations (ceased star formation and AGN feedback; Table 1 in Munari et al. 2013) and galaxies as tracers. Accordingly, the parameters  $A_{\text{ID}} = 1169.75 \pm 11.45$  and  $\alpha = 0.3593 \pm 0.0068$  were used to calculate  $M_{200}$ , the mass within which the mean matter density is 200 times  $\rho_c(z)$ , using

$$\frac{\sigma_{\text{ID}}}{\text{km s}^{-1}} = A_{\text{ID}} \left[ \frac{h(z) M_{200}}{10^{15} M_{\odot}} \right]^{\alpha}. \quad (2)$$

In Eq. (2),  $\sigma_{\text{ID}}$  denotes the line-of-sight velocity dispersion, and  $h(z)$  is the Hubble parameter at the cluster redshift  $z$  normalized by  $100 \text{ km s}^{-1} \text{ Mpc}^{-1}$ . The uncertainties for  $M_{200}$  are based on the intrinsic error of the fitting parameters and our error of  $\sigma$  for each galaxy cluster.

To compute  $r_{200}$ , the radius within which the mean density of the halo is 200 times  $\rho_c(z)$ , we used

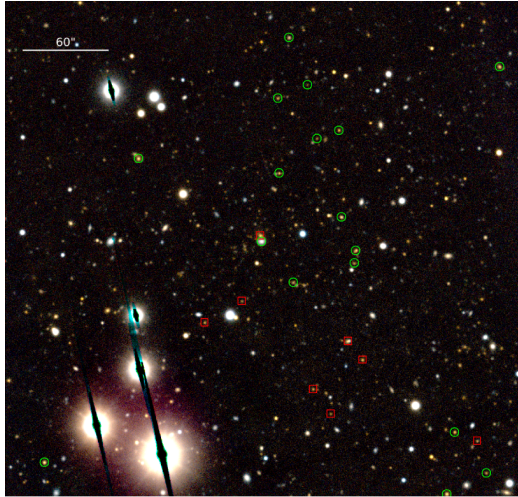
$$r_{200} = \sqrt[3]{\frac{3\pi}{4} \frac{M_{200}}{200\rho_c(z)}}, \quad (3)$$

assuming a mean density and spherical symmetry.

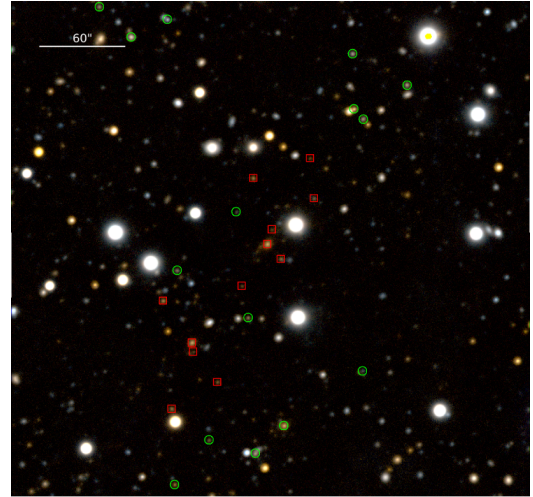
These equations are valid when we assume that the clusters are in hydrostatic equilibrium and are spherically symmetric. Such estimates are therefore only considered as proxies. The main results from the spectroscopy on clusters are summarized in Table 2, while the individual galaxy redshifts are given in Appendix A.

## 6.2. X-ray fluxes and temperatures

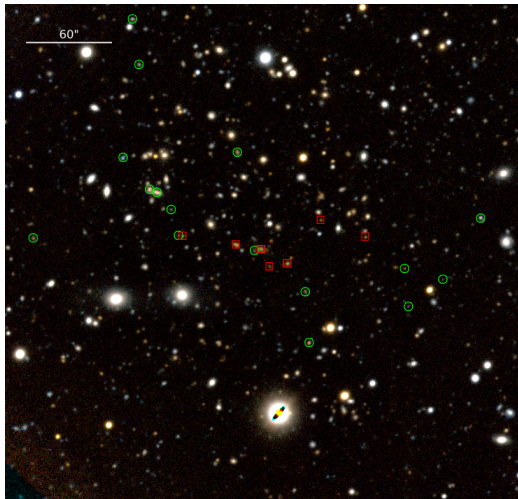
X-ray spectroscopy was carried out for all clusters with redshift known either from the literature or from this work. Source extraction regions were centred on the positions of the detected extended source in the 3XMM-DR6 catalogue (see Table 1) and set to the common radius of 300 kpc for the respective cluster redshift. Using the [0.5–3.0 keV] EPIC images, we searched for suitable background regions at approximately the same off-axis distances as the source, with a strong preference for the same chip whenever possible, and a radius sufficiently large in order to increase the quality and statistics of the background. Obvious point sources contaminating the background region were excluded. Taking the source radius into account, the background and source spectra for the individual instruments were



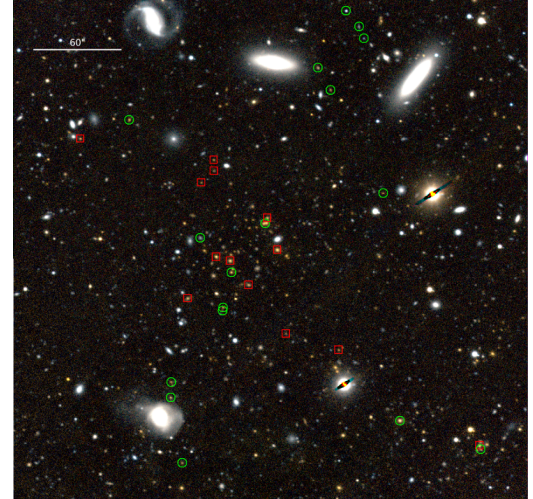
(a) 2XMMp J083026.2+524133



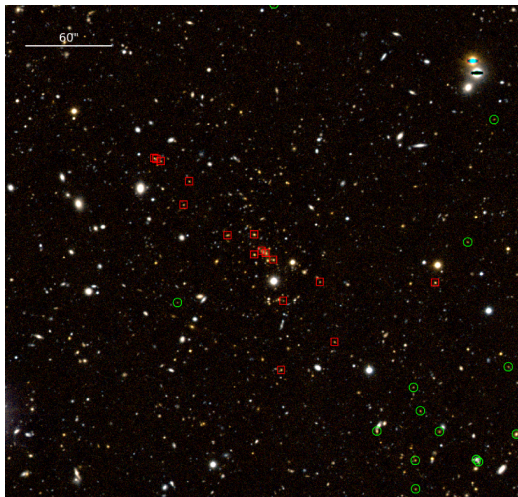
(b) 2XMMp J093437.4+551340



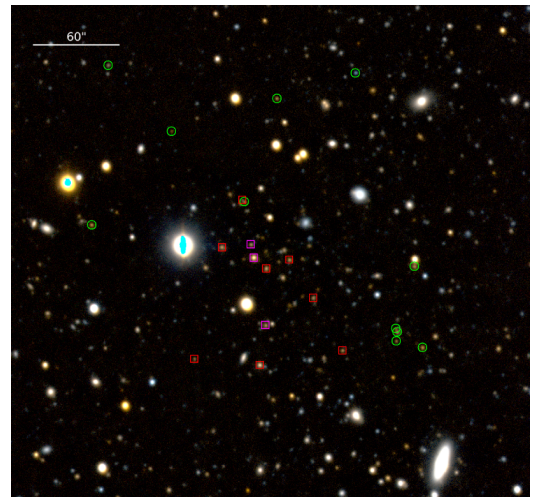
(c) 2XMMp J105319.8+440817



(d) 2XMMp J120815.5+250001



(e) 2XMMp J123759.3+180332



(f) 2XMMp J133853.9+482033

**Fig. 2.** LBC colour images of the confirmed cluster fields of Sect. 6.3. We assigned  $r$ -SLOAN and  $z$ -SLOAN images from the LBC to the blue and red channel of the colour image. The green channel was created from the mean of both bands. Overplotted red squares and green circles show cluster galaxies and spectroscopic sources outside our membership criteria, respectively. In *panel f*, which shows the cluster 2XMMp J133853.9+482033, we additionally highlight with purple squares the group of galaxies that was ruled out by the iterative sigma-clipping method (compare Sect. 6.3.6). North is up, east is left, and the images are centred on the respective X-ray position.

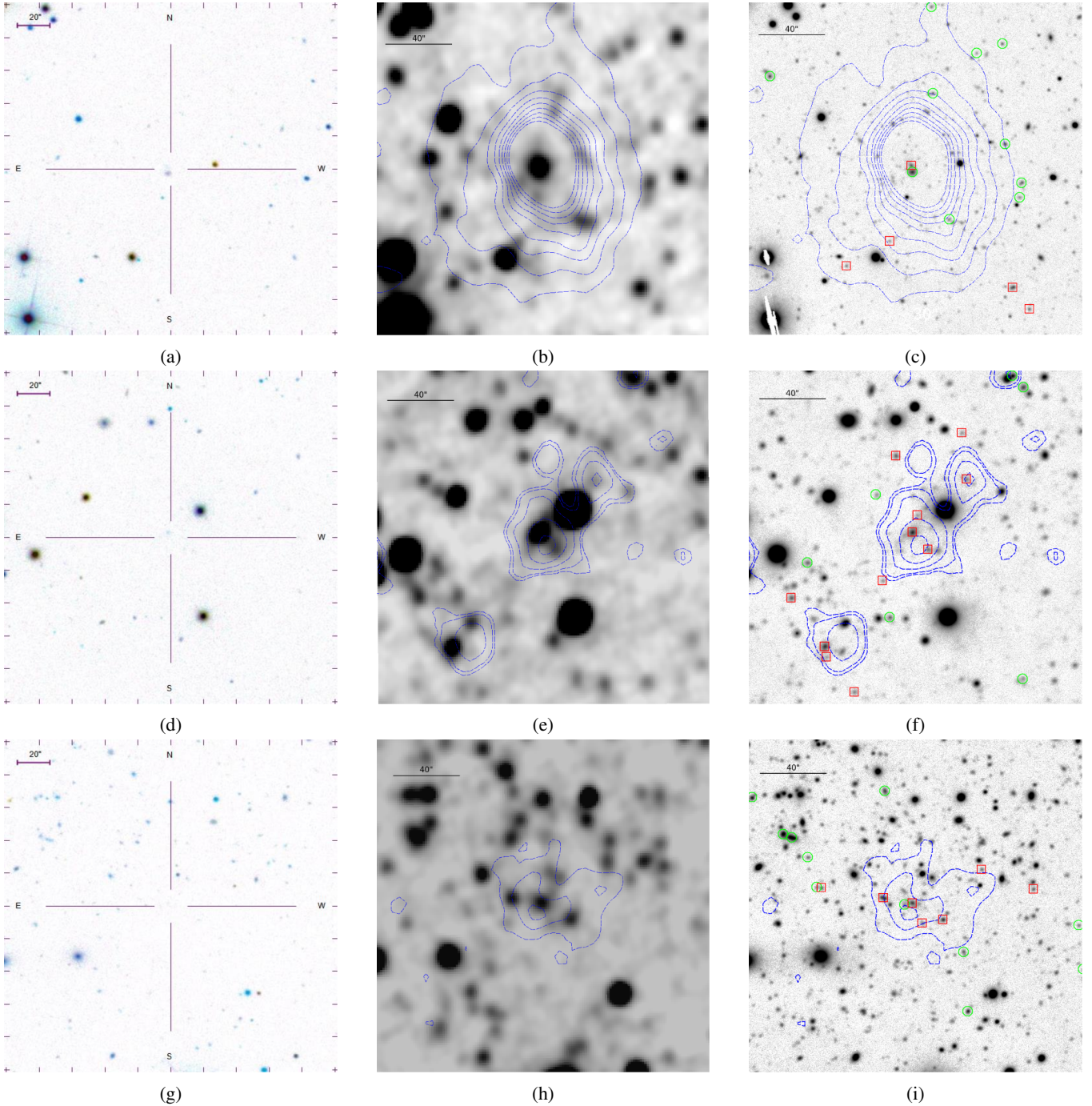


**Fig. 3.** Optical and near-IR images of the fields of 2XMMp J083026.2+524133 (*top row*), 2XMMp J093437.4+551340 (*middle*), and 2XMMp J105319.8+440817 (*bottom*). The first column shows SDSS cutouts of the respective fields, the central column shows the W1-band ( $3.4 \mu\text{m}$ ) images from the AllWISE survey, and on the right side, we present LBC images (mean of the  $r$ - and  $z$ -SLOAN filters). Images of each row are centred at the respective X-ray positions and show the same region of the sky. Blue dashed lines (*middle and right images*) indicate contours from the X-ray flux, where the levels are chosen for illustration alone. Red squares and green circles are overplotted on the LBC images, referring to cluster galaxies and spectroscopic sources outside our membership criteria, respectively. North is up, east is left, and the images are centred on the respective X-ray position.

extracted and response matrix files were created using the SAS task `especget`.

The photons of all spectra were binned to at least one count per bin with the FTOOL task `grppha`. We used the XSPEC version 12.9.0 m (Arnaud 1996), the abundance table of Wilms et al. (2000), and the atomic cross-sections of Verner et al. (1996). In order to derive the ICM temperature of the selected clusters, we fitted the extracted EPIC spectra using the APEC model (Smith et al. 2001), while we

accounted for the Galactic absorption with the `tbabs` model (Tübingen-Boulder ISM absorption model; Wilms et al. 2000), taking the column density of neutral hydrogen as a parameter (see below). For each fit we fixed the following parameters in order to reduce the number of free variables: (i) the metallicity; (ii) the column density of Galactic neutral hydrogen; and (iii) the redshift of the cluster. The value for (i) was fixed to  $Z = 0.23 \pm 0.01 Z_{\odot}$  for the whole sample of X-ray data. This value was computed by McDonald et al. (2016) in their analysis

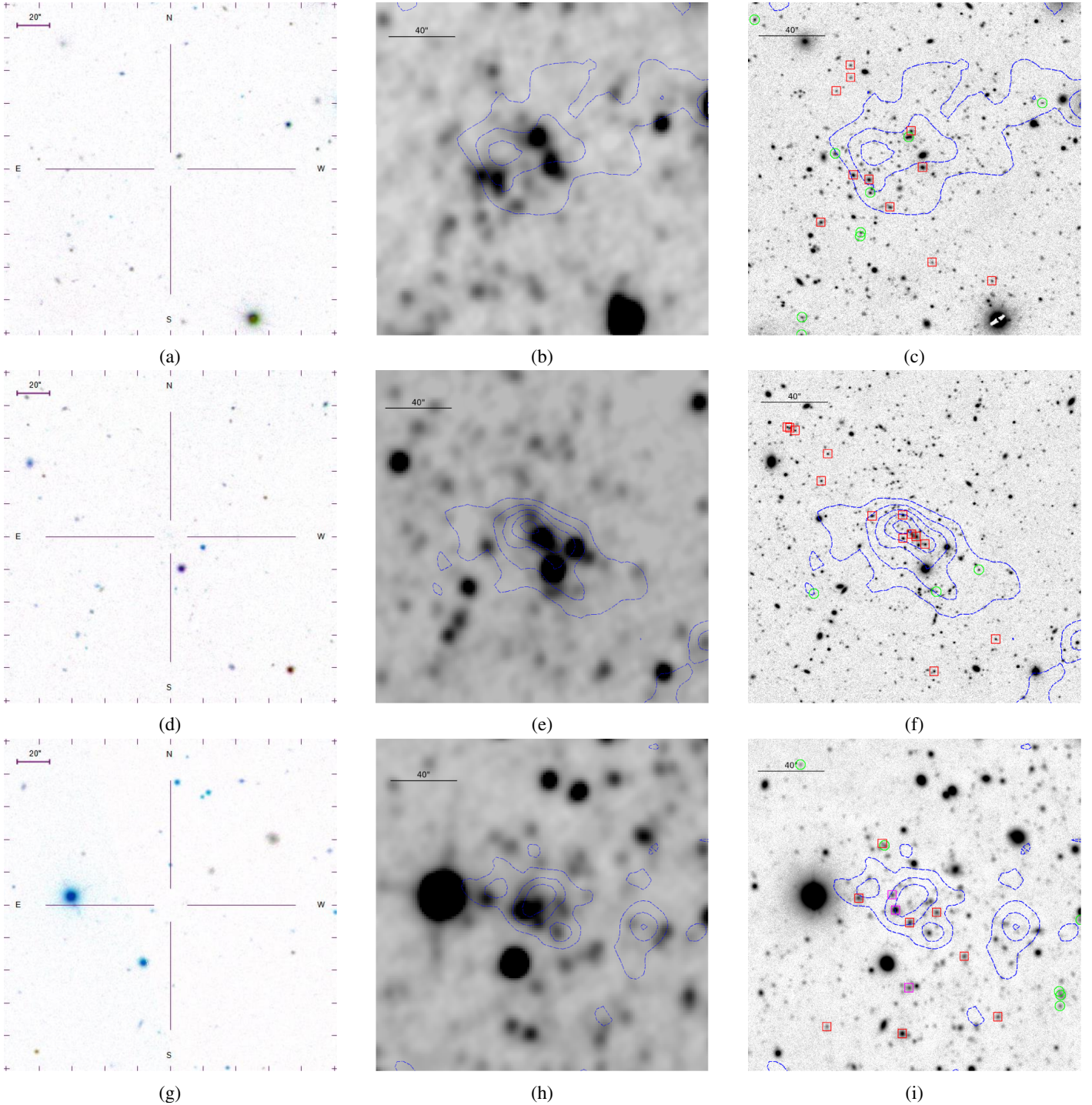


**Fig. 4.** Optical and near-IR images of the fields of 2XMMp J120815.5+250001 (*top row*), 2XMMp J123759.3+180332 (*middle*), and 2XMMp J133853.9+482033 (*bottom*). The *first column* shows SDSS cutouts of the respective fields, the *central column* the W1-band ( $3.4 \mu\text{m}$ ) images from the AllWISE survey, and on the *right side* we present LBC images (mean of the  $r$ - and  $z$ -SLOAN filters). Images of each row are centered at the respective X-ray positions and show the same region of the sky. Blue dashed lines (*middle and right images*) indicate contours from the X-ray flux, where the levels are chosen for illustration alone. Red squares and green circles are overplotted on the LBC images, referring to cluster galaxies and spectroscopic sources outside our membership criteria, respectively, while purple squares in *panel i* are explained in Sect. 6.3.6. North is up, east is left, and the images are centered on the respective X-ray position.

of 153 mass-selected galaxy clusters between  $0 < z < 1.5$ . We used the nH tool provided by HEASARC<sup>2</sup>, which determines the weighted average column density of neutral Galactic

<sup>2</sup> <https://heasarc.gsfc.nasa.gov/cgi-bin/Tools/w3nh/w3nh.pl>

hydrogen (ii) based on data by the Leiden/Argentine/Bonn (LAB) survey (Kalberla et al. 2005; Hartmann & Burton 1997). For (iii) we queried the literature for existing redshifts of our cluster candidates in addition to the clusters with spectroscopic redshifts based on data of this work (see Table 1). The best-fitting parameters, cluster temperature, the normalization,

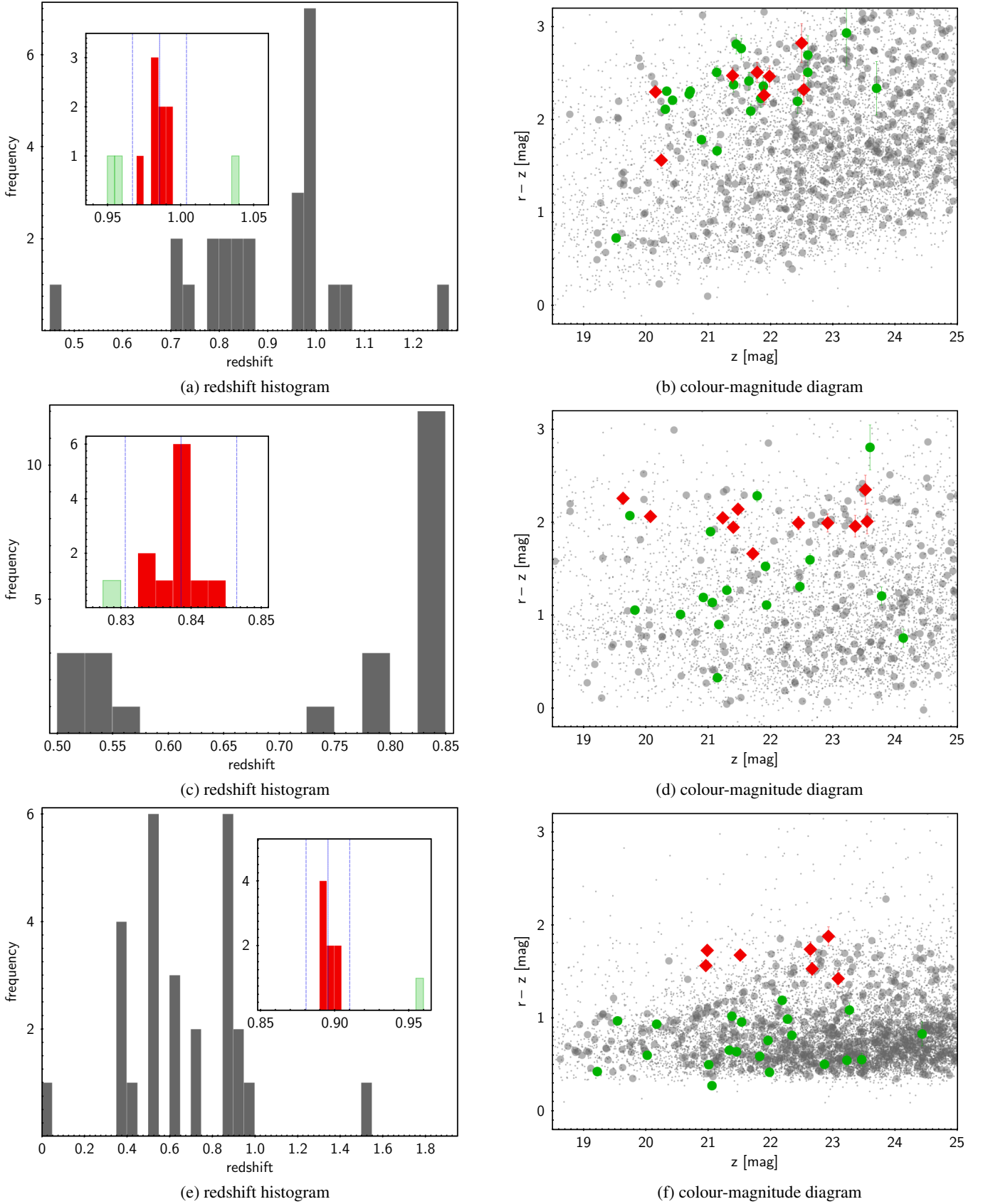


**Fig. 5.** Redshift histograms (*left side*) and colour–magnitude diagrams (*right side*) of 2XMMp J083026.2+524133 (*top*), 2XMMp J093437.4+551340 (*middle*), and 2XMMp J105319.8+440817 (*bottom*). Objects with spectra are plotted in green, while the confirmed cluster members are shown in red. Error bars plotted in the colour–magnitude diagrams indicate the photometric uncertainties and are visible when they exceed the symbol size.

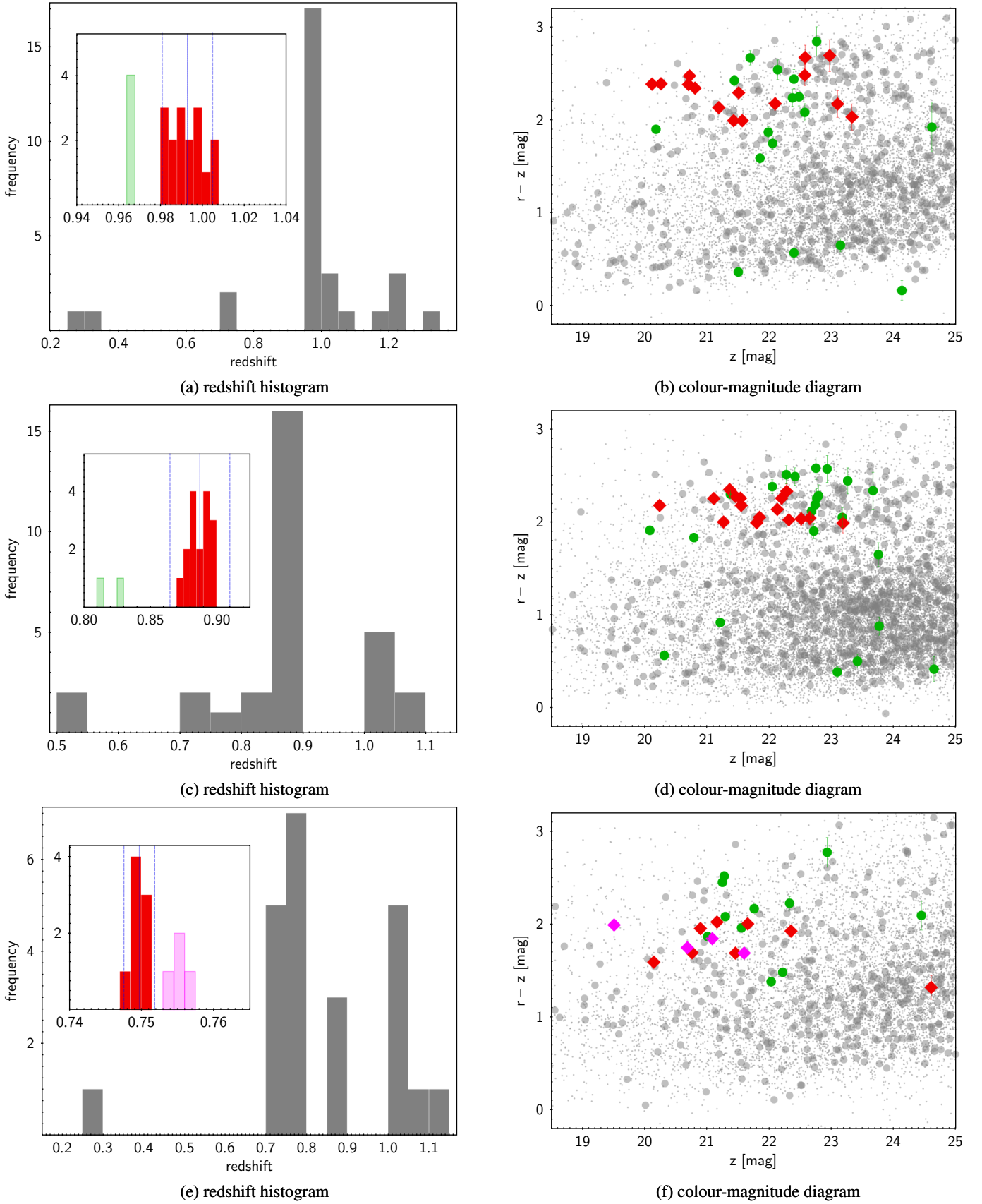


**Fig. 6.** Redshift histograms (*left side*) and colour-magnitude diagrams (*right side*) of 2XMMp J120815.5+250001 (*top*), 2XMMp J123759.3+180332 (*middle*), and 2XMMp J133853.9+482033 (*bottom*). Objects with spectra are plotted in green, while the confirmed cluster members are shown in red. Error bars plotted in the colour-magnitude diagrams indicate the photometric uncertainties and are visible when they exceed the symbol size. Galaxies excluded by the iterative sigma clipping method are shown in purple in *panels e* and *f*.

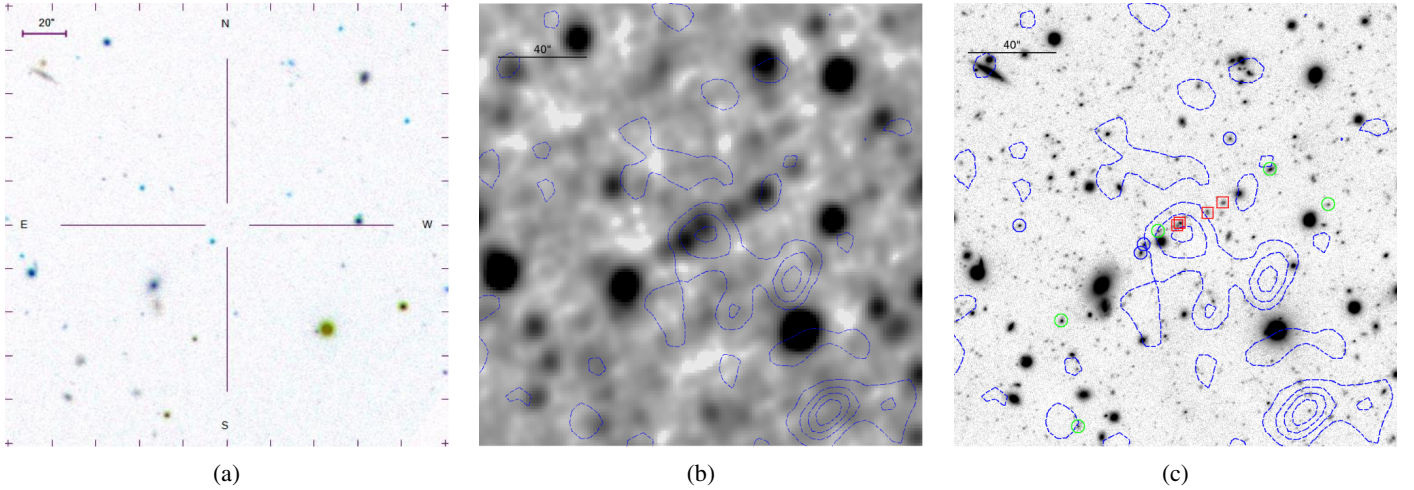


**Fig. 7.** Optical and near-IR images of the field of 2XMMp J092120.2+371735. *Panel a:* SDSS DR6 image. *Panel b:* W1-band ( $3.4 \mu\text{m}$ ) image from the AllWISE survey. *Panel c:* LBC image (mean of the  $r$ - and  $z$ -SLOAN filters). North is up, east is left, and all images cover the same region. Blue dashed lines (*middle and right images*) indicate contours from the X-ray flux. Red squares overlotted on the LBC image refer to the  $z \sim 1.2$  group, and green circles to spectroscopic sources outside our membership criteria. Blue cycles show galaxies from the foreground population ( $z \sim 1$ ).

and their respective  $1\sigma$  errors were determined by minimizing the C-statistics. The spectral fit enabled calculating the X-ray flux and luminosity in the energy range [0.5–2.0 keV]. The luminosity was further converted into a bolometric luminosity ([0.1–50 keV]) using a dummy response matrix. The derived fluxes,  $F_{0.5-2}(300 \text{ kpc})$ , and (bolometric) luminosities,  $L_{0.5-2}(300 \text{ kpc})$  and  $L_{\text{bol}}(300 \text{ kpc})$ , take into account photons emitted within the extraction region of 300 kpc. In order to derive  $L_{\text{bol}}$  for the more physically motivated radius  $r_{500}$ , we used the iterative procedure based on  $L - T$  and  $L - M$  relations published by Pratt et al. (2009). The whole procedure is outlined in detail in Takey et al. (2011), but can be summarized to work as follows. It calculates a  $M_{500}$  from the input bolometric luminosity, used to derive a first guess of  $r_{500}$  based on the  $L - M$  relation. The temperature from the  $L - T$  relation is then used to calculate the core radius of the  $\beta$  model (see relations in Finoguenov et al. 2007). The flux ratio between the input radius and the aperture extrapolated from the  $\beta$  model is finally used to correct the bolometric luminosity for the next iteration.

We present the X-ray properties of the ICM-temperature,  $F_{0.5-2}(300 \text{ kpc})$  and  $L_{\text{bol}}(r_{500})$ , and their  $1\sigma$  confidence interval in Tables 2 and 3.

### 6.3. Results of individual clusters with LBT follow-up

#### 6.3.1. 2XMMp J083026.2+524133

A redshift based on the X-ray spectrum ( $z = 0.99$ ) for this source has been published by Lamer et al. (2008).

In the follow-up imaging of the field, many faint galaxies of similar colour to the apparent BCG are visible (compare Fig. 2a), the colour–magnitude diagram in Fig. 5b indicates no dominant red sequence, and the spectroscopic follow-up revealed only eight galaxies matching our criteria for cluster members (Fig. 5a). Nevertheless, we were able to determine a mean cluster redshift of  $z = 0.9856$ , thus confirming the initial finding from Lamer et al. (2008), and a velocity dispersion (see Table 2). The dynamical mass of 2XMMp J083026.2+524133 within the radius of  $r_{200} = (2.44^{+0.79}_{-0.6}) \text{ Mpc}$  was calculated to be  $M_{200} = 5.1^{+6.7}_{-2.9} \times 10^{14} M_{\odot}$ .

The source spectrum was extracted from *XMM-Newton* observations with a total exposure time of 216.7, 223.4, and

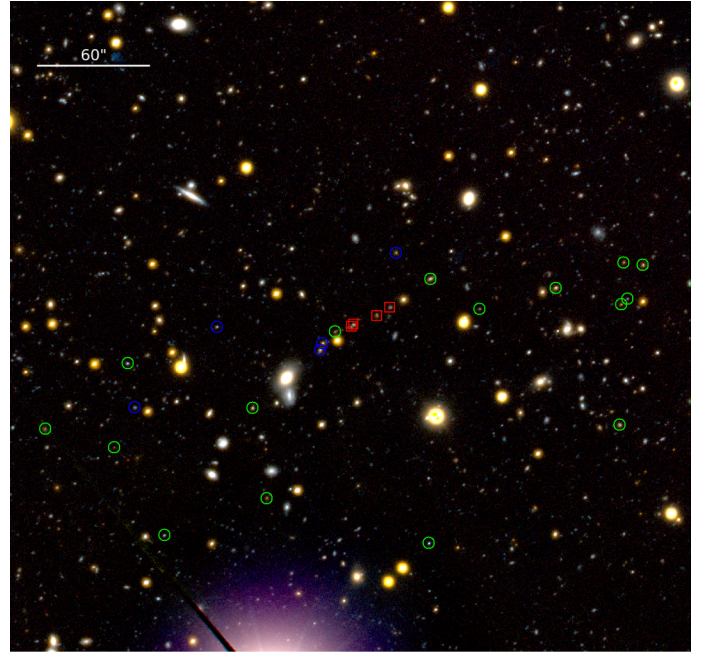


**Fig. 8.** LBC colour image of 2XMMp J092120.2+371735, the high-redshift group at  $z \sim 1.21$ . We assigned  $r$ -SLOAN and  $z$ -SLOAN images from the LBC to the blue and red channel of the colour image. The green channel was created from the mean of both bands. Overplotted red squares refer to the  $z \sim 1.2$  group, and green circles show spectroscopic sources outside our membership criteria, while blue cycles indicate galaxies of a foreground population (see Sect. 6.5.1). North is up, east is left, and the image is centred on the X-ray position.

170.3 ks for MOS1, MOS2, and PN, respectively. Owing to the high luminosity of the source ( $L_{0.5-2}(300 \text{ kpc}) = (189.6 \pm 2.8) \times 10^{42} \text{ erg s}^{-1}$ ), we were able to constrain the ICM temperature with good accuracy to  $k_B T = 7.82^{+0.4}_{-0.39} \text{ keV}$ . The temperature is in good agreement with the result from Lamer et al. (2008), which was based on fewer observations.

The high cluster mass from the dynamical analysis and the large virial radius agree within their errors with X-ray estimates

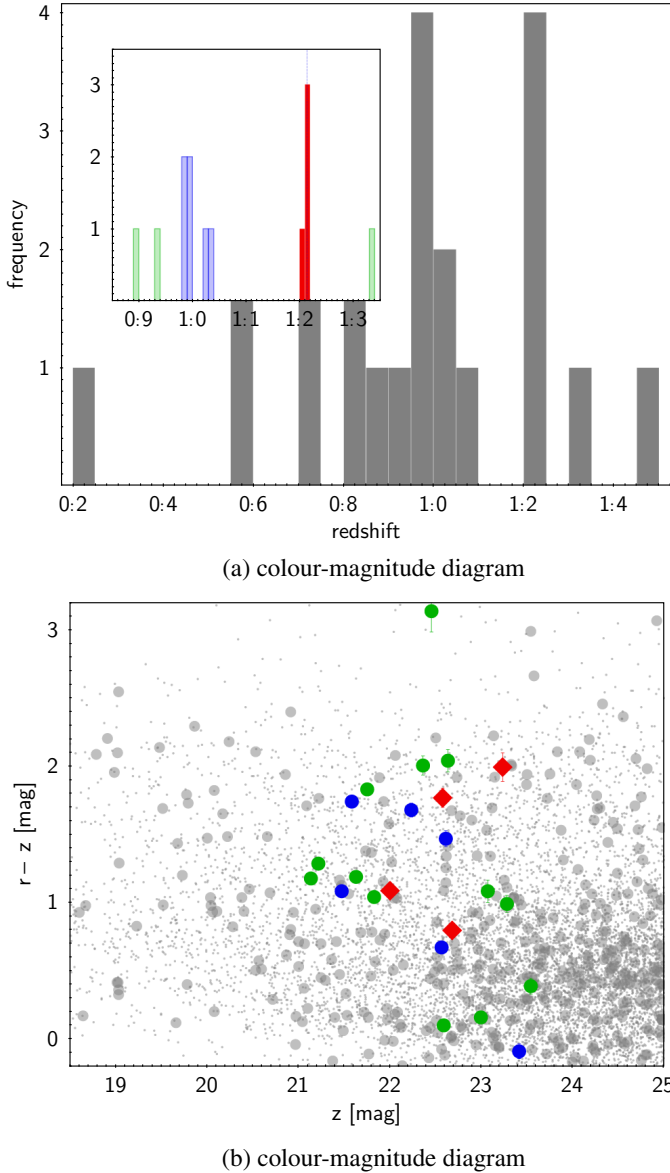


**Fig. 9.** Redshift histogram (*top panel*) and colour-magnitude diagram (*bottom*) of 2XMMp J092120.2+371735. Objects with spectra are marked green, while the members of the high-redshift group are shown in red. Blue refers to the foreground population of galaxies, which is unlikely to be responsible for the X-ray emission. Error bars plotted in *panel b* indicate the photometric uncertainties and are visible when they exceed the symbol size.

from [Lamer et al. \(2008\)](#) considering a typical scaling factor of 1.52 between  $r_{500}$  and  $r_{200}$  ([Piffaretti et al. 2011](#)).

We also note an independent cluster mass proxy from [Culverhouse et al. \(2010\)](#), who reported the gas mass derived from SZ observations. Their analysis of *XMM-Newton* data results in a cluster gas mass within  $r_{2500}$  that agrees excellently with their SZ proxy. Furthermore, [Culverhouse et al. \(2010\)](#) reported a cluster temperature of  $7.6 \pm 0.8$  keV, which exactly matches our results. Another and more recent approach using SZ measurements ([Schammel et al. 2013](#)) derived a much lower cluster mass,  $M_{200} = 3.6 \times 10^{14} M_{\odot} / 4.7 \times 10^{14} M_{\odot}$  (computed based on different models), compared to our dynamical calculation.

### 6.3.2. 2XMMp J093437.4+551340

The two-band photometry yields a tight red sequence within the field of view (compare Fig. 5d). While the optical counterpart to the BCG is hardly visible in the SDSS, AllWISE W1-imaging shows clear detections of the brightest cluster galaxies that coincide with the extended X-ray contours, see Figs. 3d, e, and f.

Optical spectroscopy resulted in 23 galaxy redshifts for the observed field. The mean cluster redshift and its velocity dispersion were calculated using an iterative clipping of redshifts from the sample (see beginning of Sect. 6) from a final census of 11 member galaxies to  $z_{cl} = 0.83858 \pm 0.00073$  and  $\sigma = (430_{-96}^{+120}) \text{ km s}^{-1}$ . In the redshift histogram (Fig. 5c), the confirmed member galaxies of galaxy cluster 2XMMp J093437.4+551340 are visible as a compact overdensity. Based on 11 cluster galaxies, a dynamical cluster mass and radius for an overdensity of  $\Delta = 200$  were computed. For these values and for the X-ray parameters of this cluster, we refer to Table 2.

The publicly available X-ray data with  $\sim 10$  ks exposure time were sufficient to determine the ICM temperature within reasonable accuracy,  $k_B T = 2.96_{-0.65}^{+0.86}$  keV, taking the spectroscopic redshift of the cluster into account. X-ray flux and luminosity were calculated to be  $F_{0.5-2}(300 \text{ kpc}) = (7.4 \pm 0.83) \times 10^{-14} \text{ erg cm}^{-2} \text{ s}^{-1}$  and  $L_{0.5-2}(300 \text{ kpc}) = (20.9 \pm 2.3) \times 10^{42} \text{ erg s}^{-1}$ , respectively (see also Table 2).

### 6.3.3. 2XMMp J105319.8+440817

When we analysed the colour-magnitude diagram (Fig. 5f) from the optical pre-imaging, a tight red sequence of galaxies became visible. Using the spectroscopic follow-up, we confirm eight galaxies out of the 28 spectra of this mask. We note that the BCG is relatively faint (20.96 mag in  $z$ -SLOAN) in comparison to the other clusters in our sample. The BCG and cluster members are not detected by the SDSS (Fig. 3g), but have IR counter-parts in the AllWISE survey (Fig. 3h).

Based on the eight identified galaxies within the redshift range of  $0.890 \lesssim z \lesssim 0.903$ , we calculated a low-precision velocity dispersion of  $\sigma = (780_{-360}^{+660}) \text{ km s}^{-1}$  (see Table 2). We also note that a close galaxy pair (the double-member east of the X-ray centre; Fig. 3i) might bias the  $\sigma$  by possible interaction. Spectra of both galaxies were taken from the same slit on the MOS-mask and appear only  $\sim 1.8''$  and  $\sim 2950 \text{ km s}^{-1}$  apart in projection and recessional velocity, respectively.

As a peculiarity within the cluster field, imaging revealed a slightly distorted blue object only  $\sim 5''$  away from the BCG. We identified this object as a background galaxy and were able to assign a redshift of  $z = 3.8354$ . The object is not bent to an Einstein ring, nor were any possible multiple images to this galaxy identified. Based on its magnitude (22.3 mag in  $z$ ) with respect to its high redshift and the apparent magnitudes of the cluster members at  $z = 0.8955$  (compare Table A.1), the galaxy is most likely lensed by the BCG of the galaxy cluster.

In the XSA we found two observations covering the source 2XMMp J105319.8+440817 with cleaned exposure times between 4 and 11 ks (Table D.1). Using our common procedure, we extracted an X-ray flux of  $F_{0.5-2}(300 \text{ kpc}) = (2.37 \pm 0.27) \times 10^{-14} \text{ erg cm}^{-2} \text{ s}^{-1}$  and a model luminosity of  $L_{0.5-2}(300 \text{ kpc}) = (76.7 \pm 8.7) \times 10^{42} \text{ erg s}^{-1}$ . The best-fitting value for the gas temperature of the cluster was calculated to be  $k_B T = 3.6_{-0.76}^{+1.2}$  keV (Table 2).

### 6.3.4. 2XMMp J120815.5+250001

In the LBC imaging data, very many galaxies around the centre of 2XMMp J120815.5+250001 are visible (compare Fig. 2d). The colour–magnitude diagram in Fig. 6b appears to have a rich red sequence, which is not very tight in colour. Within the MODS field of view of 2XMMp J120815.5+250001, we spectroscopically identified 20 galaxies in the redshift range of  $0.96 < z < 1.06$ . A cluster consisting of those 20 galaxies would exhibit line-of-sight velocities ( $|v_{\text{los}}| > 6000 \text{ km s}^{-1}$ ) that are too high for this to be considered a gravitationally bound system. We detect several bright galaxies with greatly different recessional velocities near the centre of the elongated X-ray emission (Fig. 4c), imaged as the brightest four galaxies near the inner X-ray contour. When we consider each as a possible BCG, we obtain different samples of cluster members and velocity dispersions, regarding our member selection algorithm. All four bright galaxies appear related to red sources (W1–W2 between 0.22 and 0.35) in the AllWISE data, visible as bright sources in Fig. 4b, and thus give no clear indication of a single BCG.

In the following, we consider the galaxy at the position 12:08:15 +25:00:01 with a  $z$ -SLOAN magnitude of 20.262 mag and a distance of  $5''$  with respect to the X-ray centre, as the proper BCG. Our algorithm estimates a cluster redshift of  $z = 0.9929 \pm 0.0026$  and  $\sigma = (1200^{+300}_{-240}) \text{ km s}^{-1}$ , taking the 16 galaxies into account as cluster members. The respective radius and mass we determine are listed in Table 2.

We extracted source spectra for all EPIC instruments using the one *XMM-Newton* observation available for this cluster. The APEC model fit constrained the ICM temperature for 2XMMp J120815.5+250001 to be  $kT = 4.1^{+2.2}_{-1.1} \text{ keV}$ . X-ray flux and luminosity were calculated to be  $F_{0.5-2}(300 \text{ kpc}) = (2.79 \pm 0.42) \times 10^{-14} \text{ erg cm}^{-2} \text{ s}^{-1}$  and  $L_{0.5-2}(300 \text{ kpc}) = (106 \pm 16) \times 10^{42} \text{ erg s}^{-1}$ , respectively.

The velocity dispersion of this cluster may be contaminated by galaxies that are not bound to the cluster, but are part of a larger structure. This is further supported by the relatively low ICM temperature found from the analysis of EPIC spectra compared to the large  $\sigma$  from optical spectroscopy.

### 6.3.5. 2XMMp J123759.3+180332

The source 2XMMp J123759.3+180332 appears very rich in red galaxies in the optical pre-imaging (Fig. 2e), with an apparent concentration in the central part of the X-ray emission (Fig. 4f), and bright and possibly blended IR emission in the AllWISE imaging data (Fig. 4e). The optical richness is also recovered in the corresponding colour–magnitude plot (Fig. 6d) as a clearly visible red sequence, of which a considerable fraction of objects were confirmed as cluster members. Applying our clipping algorithm, we were able to identify 16 members within the redshift range of  $0.865 \lesssim z \lesssim 0.9$ , and consequently fixed the cluster redshift to  $z = 0.8874 \pm 0.0024$  with  $\sigma = (1200^{+310}_{-250}) \text{ km s}^{-1}$ . The dynamical cluster mass computed based on  $\sigma$  results in a high value and confidence interval. A high cluster mass, however, slightly contradicts the average X-ray temperature (compare Table 2). The population of cluster member galaxies might contain an unidentified fraction of interloping galaxies, which we cannot identify for statistical reasons.

The LBC data imaged two blue objects in the cluster field (highlighted as blue circles in Fig. 2e) with an apparently bent morphology. The respective spectra of both sources show no clear emission or absorption feature, rendering no opportunity

to determine redshifts. A clear similarity between both spectral shapes is obvious, on the other hand, substantiating the hypothesis that both objects are lensed images of a source with a redshift in the redshift desert between  $1.4 < z < 2.0$ .

X-ray source photons of 2XMMp J123759.3+180332 were extracted within a radius of  $\sim 0.95 \text{ Mpc}$ . The low number of photons from the source (63/102/73 counts for MOS1/MOS2/PN) resulted in large error margins for the ICM temperature:  $k_B T = 5.0^{+1.9}_{-1.1} \text{ keV}$ . The extracted flux was derived to be  $F_{0.5-2}(300 \text{ kpc}) = (4.75 \pm 0.47) \times 10^{-14} \text{ erg cm}^{-2} \text{ s}^{-1}$ , and using the cluster redshift from optical spectroscopy, we calculated the X-ray luminosity to be  $L_{0.5-2}(300 \text{ kpc}) = (134 \pm 13) \times 10^{42} \text{ erg s}^{-1}$ .

### 6.3.6. 2XMMp J133853.9+482033

The LBT imaging shows the field of 2XMMp J133853.9+482033 as a rich cluster of galaxies. However, the red sequence (Fig. 6f) is not very pronounced. We identified the brightest galaxy near the X-ray centre as BCG (magenta square in Fig. 4i), and the initial sample of tentative cluster galaxies comprises 13 galaxies within  $0.749 \lesssim z \lesssim 0.756$ . Our iterative member clipping, however, divides the sample into two groups, indicated by red and magenta bars in the redshift histogram in Fig. 6e. The method finally excludes the initial BCG and surrounding group of galaxies (magenta) from the sample of cluster member galaxies (red) during the iteration. We therefore note that the following estimates are most possibly biased by insufficient member statistics. With to the procedure we applied for the whole spectroscopic sample in this paper, we calculate a mean cluster redshift based on eight galaxies of  $z = 0.74969 \pm 0.00030$  and a velocity dispersion of  $\sigma = (122^{+32}_{-26}) \text{ km s}^{-1}$ . The low-velocity dispersion shifts 2XMMp J133853.9+482033 more into the regime of galaxy groups than clusters, and results in a dynamical mass estimate of only  $M_{200} = 1.3^{+1.4}_{-0.6} \times 10^{12} M_{\odot}$ . We summarize all properties in Table 2.

We were unable to constrain the gas temperature of 2XMMp J133853.9+482033 based on the publicly available X-ray data. The X-ray flux and luminosity were measured to be  $F_{0.5-2}(300 \text{ kpc}) = (1.1 \pm 0.16) \times 10^{-14} \text{ erg cm}^{-2} \text{ s}^{-1}$  and  $L_{0.5-2}(300 \text{ kpc}) = (18.8 \pm 2.8) \times 10^{42} \text{ erg s}^{-1}$ .

## 6.4. Results: galaxy clusters with redshifts from the literature

This section summarizes results from the subsample of X-ray selected cluster candidates, which are known to be clusters in the literature. We queried the NED for publications on galaxy clusters and took advantage of their spectroscopic cluster redshifts for our APEC fit of the analysis of *XMM-Newton* data. Our goal was to calculate X-ray cluster properties such as ICM temperature, flux, and luminosity for this sample as well and compare our *XMM-Newton* based properties to the literature values. We refer to Sect. 7, where we show an  $L - T$  plot of all clusters within this sample. In Table D.1 we collect important data on the individual cluster detection, including available OBSIDs, cleaned exposure times based on our reduction, and the 2XMMp vs. 3XMM-DR6 cross-reference. The procedure of our X-ray data reduction and analysis is described in Sects. 5 and 6.2, respectively.

**Table 3.** X-ray properties for clusters with spectroscopic redshift from the literature.

Name	$z_{\text{lit}}$	$F_{0.5-2}(300 \text{ kpc})$ [ $10^{-14} \text{ erg cm}^{-2} \text{ s}^{-1}$ ]	$L_{\text{bol}}(r_{500})$ [ $10^{42} \text{ erg s}^{-1}$ ]	$k_{\text{B}}T$ [keV]	reference
2XMMp J030212.0-000133	1.185	$0.884 \pm 0.097$	$162 \pm 17$	$4.7^{+1.5}_{-0.9}$	Šuhada et al. (2011)
2XMMp J084836.4+445345	1.273	$0.406 \pm 0.059$	$75 \pm 12$	$2.5^{+1.4}_{-0.6}$	Stanford et al. (1997)
2XMMp J084858.3+445158	1.261	$0.885 \pm 0.053$	$192 \pm 12$	$4.93^{+0.77}_{-0.62}$	Rosati et al. (1999)
2XMMp J100451.6+411626	0.836	$6.65 \pm 0.17$	$664 \pm 13$	$4.84^{+0.31}_{-0.3}$	Hoeft et al. (2008)
2XMMp J105344.2+573517	1.134	$1.928 \pm 0.038$	$362.7 \pm 3.6$	$4.52^{+0.24}_{-0.22}$	Hashimoto et al. (2005)
2XMMp J123113.1+154550	0.893	$3.89 \pm 0.3$	$609 \pm 32$	$8.9^{+4.1}_{-2.2}$	Rabitz et al. (in prep.)

**Notes.** The X-ray properties flux (Col. 3) and temperature (Col. 5) were measured within radii of 0.3 Mpc at the redshift of the cluster, where we used the spectroscopic redshifts available from the reference noted in Col. 6. The bolometric luminosity (Col. 4) was extrapolated to  $r_{500}$  (for details, see Sect. 6.2). The X-ray flux is given in units of  $10^{-14} \text{ erg cm}^{-2} \text{ s}^{-1}$ , and the luminosity in  $10^{42} \text{ erg s}^{-1}$ .

#### 6.4.1. 2XMMp J030212.0-000133

The cluster was discovered in X-rays in the framework of the *XMM-Newton* Distant Cluster Project (XDCP; Fassbender et al. 2011). From six member galaxy spectra, Šuhada et al. (2011) derived a cluster redshift of  $z = 1.185 \pm 0.016$ , which we adopted for our X-ray analysis.

We extracted the X-ray spectrum within 300 kpc in the available  $\sim 47$  and  $\sim 37$  ks exposures of MOS1/MOS2 and PN, respectively. The X-ray flux and the luminosity were calculated to be  $F_{0.5-2}(300 \text{ kpc}) = (0.884 \pm 0.097) \times 10^{-14} \text{ erg cm}^{-2} \text{ s}^{-1}$  and  $L_{0.5-2}(300 \text{ kpc}) = (35.2 \pm 3.9) \times 10^{42} \text{ erg s}^{-1}$ , and the cluster temperature was fitted to  $k_{\text{B}}T = 4.7^{+1.5}_{-0.9} \text{ keV}$ . Flux and luminosity agree within  $3\sigma$  with those derived by Šuhada et al. (2011), which are based on an extraction radius of  $55''$ . The ICM temperature is higher in our case but is based on the spectral fits, while Šuhada et al. (2011) estimated their  $T_{500}$  according to scaling relations. Our X-ray properties are summarized in Table 3.

#### 6.4.2. 2XMMp J084836.4+445345 and 2XMMp J084858.3+445158

We now describe together the properties of two single extended X-ray detections.

Numerous publications in addition to the initial discovery papers (Stanford et al. 1997; Rosati et al. 1999) are available for these two clusters, for which more recent work suggested the terminus supercluster because of their close neighbourhood in on-sky projection and in redshift space (compare Mei et al. 2012). Since they were initially found as extended sources in the RDCS, first X-ray fluxes and luminosities are based on ROSAT data. Observations with *Chandra* (i.e. Stanford et al. 2001) helped to reject point-sources from the data analysis because of their increased spatial resolution, and this improved the quality of the parameters derived for the clusters. On the other hand, *Chandra* results show a large spread, at least partly caused by the different calibration of the low-energy QE degradation as summarized and detailed by Jee et al. (2006).

Our X-ray analysis is based on *XMM-Newton* data and not directly comparable to previous results because of cross-calibration issues between *XMM-Newton* and *Chandra*. We used all observations included in Table D.1, covering the fields of 2XMMp J084836.4+445345 (Lynx-W) and

2XMMp J084858.3+445158 (Lynx-E). For Lynx-W, we extracted source photons within 0.3 Mpc for the MOS1/MOS2 and PN instruments, leading to  $F_{0.5-2}(300 \text{ kpc}) = (0.406 \pm 0.059) \times 10^{-14} \text{ erg cm}^{-2} \text{ s}^{-1}$  and  $L_{0.5-2}(300 \text{ kpc}) = (30.8 \pm 4.4) \times 10^{42} \text{ erg s}^{-1}$ . The spectral model fits returned a best-fitting temperature of  $k_{\text{B}}T = 2.5^{+1.4}_{-0.6} \text{ keV}$ , where the large uncertainties reflect the low number of photons received from this cluster in X-rays. Stanford et al. (2001) calculated flux and luminosity for this cluster from a smaller extraction radius, and thus their results are not directly comparable to ours. However, our cluster temperature is comparable to their work ( $k_{\text{B}}T = 1.6^{+0.8}_{-0.6} \text{ keV}$ ), as well as to an analysis of *Chandra* data by Jee et al. (2006) ( $k_{\text{B}}T = 1.7^{+0.7}_{-0.4} \text{ keV}$ ).

The *XMM-Newton* spectral analysis for the cluster Lynx-E resulted in fluxes and luminosities of  $F_{0.5-2} = (0.885 \pm 0.053) \times 10^{-14} \text{ erg cm}^{-2} \text{ s}^{-1}$  and  $L_{0.5-2} = (50.2 \pm 3) \times 10^{42} \text{ erg s}^{-1}$ . The flux is in agreement with measurements from Stanford et al. (2001), where their aperture flux was extrapolated. Our best-fitting parameter for the ICM temperature is  $k_{\text{B}}T = 4.93^{+0.77}_{-0.62} \text{ keV}$ , which is also comparable with the results by Stanford et al. (2001) ( $k_{\text{B}}T = 5.8^{+2.8}_{-1.7} \text{ keV}$ ); a comparison with additional results based on *Chandra* data is summarized in Jee et al. (2006).

#### 6.4.3. 2XMMp J100451.6+411626

Hoeft et al. (2008) found the extended source 2XMMp J100451.6+411626 in the field of a lensed quasar (SDSS J1004+4112), and identified the cluster in deep SUBARU-imaging of the field. They noted clear visibility of extended X-ray emission in all EPIC instruments and a faint optical counter-part in the centre of the emission in the SDSS *i*-band, indicating a distant galaxy cluster. The cluster redshift they provided in their analysis ( $z = 0.82 \pm 0.02$ ) was derived from the X-ray spectrum itself.

We extracted the source within 300 kpc, corresponding to  $35.4''$ , in contrast to Hoeft et al. (2008) ( $50''$ ). No redshift based on spectroscopic data was available, but the quality of the available X-ray data allowed for a precise determination of the galaxy clusters redshift. We measured a redshift of  $z = 0.836^{+0.031}_{-0.041}$ , which agrees very well with the value given by Hoeft et al. (2008) ( $z = 0.82$ ). The resulting X-ray flux and luminosity are  $F_{0.5-2}(300 \text{ kpc}) = (6.66 \pm 0.17) \times 10^{-14} \text{ erg cm}^{-2} \text{ s}^{-1}$  and  $L_{0.5-2}(300 \text{ kpc}) = (171.1 \pm 4.4) \times 10^{42} \text{ erg s}^{-1}$ , respectively. The

temperature derived in our APEC fit,  $k_B T = 4.84^{+0.31}_{-0.30}$  keV, is also in within the  $1\sigma$  interval of the findings by [Hoeft et al. \(2008\)](#) ( $k_B T = 4.2 \pm 0.4$  keV).

#### 6.4.4. 2XMMp J105344.2+573517

The initial detection of galaxy cluster 2XMMp J105344.2+573517 was named RX J1053.7+5735 and is based on deep ( $\sim 1.3$  Ms) ROSAT observations ([Hasinger et al. 1998](#)) in a field with very low column density of the neutral galactic hydrogen ([Lockman et al. 1986](#)). The structure of the source in the so-called Lockman-Hole was found to be double-lobed in the X-ray data. Follow-up imaging in the optical and NIR uncovered potential cluster galaxies for both sides of the lobe and the peculiarity of a bright lensing arc at redshift  $z = 2.57$ , lensed by the BCG of the eastern lobe ([Thompson et al. 2001](#)). Using the Deep Imaging Multi-Object Spectrograph (DEIMOS; [Faber et al. 2003](#)) at the Keck II telescope, [Hashimoto et al. \(2005\)](#) confirmed six galaxies at concordant redshifts in both lobes of RX J1053.7+5735, giving a mean cluster redshift of  $z = 1.134$  – in good agreement with  $z \sim 1.16^{+0.02}_{-0.03}$  and  $z \sim 1.14^{+0.02}_{-0.01}$  estimated from the X-ray Fe-K line for the eastern and western lobe and based on *XMM-Newton* data ([Hashimoto et al. 2004](#)). The coinciding redshift measurements of both lobes with independent methods underlines the possibility that RX J1053.7+5735 is in fact a merging cluster system.

For the X-ray analysis in this work, we used all observations from the XSA noted in Table D.1. After cleaning for times of high background events, the summed exposure times are  $\sim 135$ ,  $\sim 147$ , and  $\sim 114$  ks for MOS1, MOS2, and PN. Our APEC model fits give a flux and rest frame luminosity of  $F_{0.5-2}(300 \text{ kpc}) = (1.928 \pm 0.038) \times 10^{-14}$  erg cm $^{-2}$  s $^{-1}$  and  $L_{0.5-2}(300 \text{ kpc}) = (106.4 \pm 2.1) \times 10^{42}$  erg s $^{-1}$ . Owing to the differences in the extraction region, these results are not directly comparable to values in the literature. The best-fitting ICM temperature according to our model,  $k_B T = 4.52^{+0.24}_{-0.22}$  keV, is in agreement with [Hashimoto et al. \(2004\)](#) and their results for the eastern and western lobe ( $3.4^{+0.2}_{-0.1}$  and  $4.4^{+0.3}_{-0.3}$ ), but also with earlier work ( $k_B T = 4.9^{+1.5}_{-0.9}$  keV, see [Hashimoto et al. 2002](#)).

#### 6.4.5. 2XMMp J123113.1+154550

The source 2XMMp J123113.1+154550 has previously been selected by the XDCP, and received deep imaging and spectroscopic follow-up with VLT/FORS2. We will present further details on the optical analysis for this cluster as part of a larger sample in an upcoming paper (Rabitz et al., in prep.). However, we use the spectroscopic mean cluster redshift of  $z = 0.893$  here to reduce the free parameter for the APEC model fit. We extracted photons of the cluster within 0.3 Mpc around the source position of 2XMMp J123113.1+154550. The best-fit parameter for the cluster temperature is  $k_B T = 8.9^{+4.1}_{-2.2}$  keV, and therefore larger than for the highly luminous cluster 2XMMp J083026.2+524133 (compare Sect. 6.3.1), but with significant uncertainties. Furthermore, flux and luminosity were computed to be  $F_{0.5-2}(300 \text{ kpc}) = (3.89 \pm 0.3) \times 10^{-14}$  erg cm $^{-2}$  s $^{-1}$  and  $L_{0.5-2}(300 \text{ kpc}) = (99.3 \pm 7.8) \times 10^{42}$  erg s $^{-1}$ , which is almost a factor of two smaller than the  $F_{0.5-2}(300 \text{ kpc})$  and  $L_{0.5-2}(300 \text{ kpc})$  of the latter highly luminous cluster. We summarize all X-ray properties of our analysis in Table 3.

## 6.5. Results: rejected and as yet unclassified fields

### 6.5.1. 2XMMp J092120.2+371735

The SDSS field of this source is empty, while WISE data show a clear signal in the central region of the X-ray emission (compare cutouts in Figs. 7a–c). LBC pre-imaging (Fig. 8) reveals a field that has no obvious overdensity of red galaxies, but is dominated by very faint sources. However, the possibility exists that the 4000 Å break is already redshifted out of the  $z$ -SLOAN band, causing no red ridge line to be present in our given filter set, which is also reflected by the colour–magnitude diagram (Fig. 9b). Since the source was considered to contain a potential high-redshift ( $z > 1$ ) cluster, an attempt to select possible member galaxies was made for the spectroscopic follow-up. Spectra of the brightest extragalactic sources near the centre of the extended X-ray emission, however, yielded two redshift overdensities, at  $z \sim 1.0$  and  $z \sim 1.2$  (corresponding to the blue and red colours; see Figs. 7c and 9).

The possible low-redshift cluster, with galaxies in the range of  $0.984 \lesssim z \lesssim 1.033$ , would result in a velocity dispersion that is too high. These galaxies are therefore not considered as a bound system. The four galaxies within the range of  $1.209 \lesssim z \lesssim 1.214$  are, however, much closer in redshift space, with their two brightest members in the very X-ray centre (Fig. 7c). We furthermore note that in the WISE IR imaging in Fig. 7b, we clearly see counterparts to the high-redshift galaxies. The four members of the high mean redshift population ( $z = 1.2134 \pm 0.0014$ ) do not form a typical red sequence (Fig. 9b), but were found to be active and are hence relatively blue galaxies according to their [OII] emission line – an indication for ongoing star formation. The X-ray emission from 2XMMp J092120.2+371735 is clearly extended ( $\sim 13''$  in 3XMM-DR6; compare Table D.1), and a meaningful tbabs fit of the extracted spectra was not possible, given the quality of the archival data. Because only four galaxies with coinciding redshifts are confirmed and we lack a clear detection of a red-sequence or even a passive BCG, we cannot confirm the status of a galaxy cluster for this group of  $z \sim 1.21$  galaxies.

### 6.5.2. 2XMMp J093607.2+613245

The X-ray source 2XMMp J093607.2+613245 is catalogued as an extended source in 2XMMp, and its extent is also confirmed by the 3XMM-DR6 catalogue. Deep imaging with the LBC shows only faint blue galaxies within the central X-ray emission region, with a WISE counterpart in the W1 band (see upper panel in Fig. C.2), while survey data from the SDSS do not detect foreground sources. Spectroscopic follow-up with MODS revealed three galaxies within a relatively wide redshift range ( $z = 0.81 \dots 0.84$ ), including the galaxy closest to the X-ray position, an OII emitter at  $z = 0.811$ . An object at  $12''$  angular distance from the X-ray position was identified as a QSO at  $z = 1.55$ . A re-inspection of the X-ray source showed that the 2XMMp source is a blend of two sources to which the QSO contributes part of its flux. Since it remains unclear whether the galaxies at  $z \sim 0.83$  form a cluster that could give rise to the remaining X-ray emission, we did not add this source to the sample of identified clusters.

### 6.5.3. 2XMMp J120735.1+250538

The X-ray emission related to 2XMMp J120735.1+250538 is of low extent ( $6.6''$ ) and blended with a point source. Because

of the uncertain X-ray extent and the lack of obvious member galaxies, spectroscopic follow-up was not executed.

#### 6.5.4. 2XMMp J133038.6-013832

The X-ray emission of 2XMMp J133038.6-013832 is of relatively low extent ( $\sim 6.8''$ ; see Table D.1) and well isolated. In the centre, LBC imaging detects a concentration of red galaxies with counterparts in WISE data (see Figs. C.2i and h). We skipped further follow-up for this cluster candidate, since its BCG is already visible in newer releases of the SDSS, where it is listed with a photometric redshift of  $z \sim 0.75$  and has a magnitude of 19.92 in the  $z$ -band of the LBC pre-imaging. This renders a high-redshift nature unlikely.

#### 6.5.5. 2XMMp J144854.8+085400

This X-ray source is clearly extended in the softer XMM-EPIC images [0.2–2] keV. In the harder bands, at [2.0–12] keV, a point source is apparent near the centre of the soft extended emission. No obvious galaxy cluster can be found in the LBC imaging. However, the hard point source is identified with a galaxy that is also detected in the SDSS with  $m_r = 22.64$  and has a photometric redshift  $z_{\text{ph}} = 0.75$ . A search in radio catalogues of the field revealed two 1.4 GHz NVSS (Condon et al. 1998) sources  $\approx 1$  arcmin east and west of the hard X-ray source, roughly corresponding to the elongation of the extended X-ray emission. The 5 GHz FIRST survey (Becker et al. 1994) also shows several compact and extended sources, and the low-frequency GLEAM survey (Hurley-Walker et al. 2017) detected one source near the position of the eastern NVSS source.

We therefore conclude that the extended X-ray emission is more likely associated with emission from the jets of a radio-loud AGN in the galaxy at  $z_{\text{ph}} = 0.75$ . The core of the AGN must be highly obscured, since it is not visible at soft X-rays below 2 keV.

#### 6.5.6. 2XMMp J145220.8+165458

In the 2XMMp catalogue, 2XMMp J145220.8+165458 is listed as an extended source, but it has lost the extent flag in the more recent 3XMM-DR6 catalogue. The central part of the X-ray emission harbours a galaxy that was also visible in the SDSS. Deep LBC imaging and IR data from WISE do not indicate an additional background overdensity of galaxies (compare Fig. C.1e and the middle panel of Fig. C.3). Therefore the source 2XMMp J145220.8+165458 was rejected as high-redshift galaxy cluster and excluded from the follow-up program.

#### 6.5.7. 2XMMp J151716.8+001302

The source of 2XMMp J151716.8+001302 is extended in both 2XMMp and 3XMM-DR6, considering the OBSID 0103860601. A following observation (0201902001), only present in the more recent catalogue, lists no extent for this source, hence it remains uncertain whether the source is extended at all. The deep imaging with the LBC and survey data of WISE do not indicate a population of high-redshift galaxies either. Therefore this source was removed from the list of tentative high-redshift galaxy clusters.

## 6.6. Results: $L - T$ relation

Based on the X-ray properties derived for the confirmed clusters of galaxies, we analysed the relation between  $L_{\text{bol}}(r_{500})$  and  $k_{\text{B}}T$ . The bolometric luminosities within the radius  $r_{500}$  were calculated using an iterative method (Takey et al. 2013), and the cluster temperatures were derived from spectral model fits to the innermost 300 kpc region of the cluster, which we described in Sect. 6.2. We note that the spatial resolution of *XMM-Newton* does not allow us to exclude the core of clusters at the high redshifts of our sample, and therefore ICM temperatures might be biased by a cool cluster core. When we analysed our combined sample of 11 clusters (Tables 2 and 3) using the BCES orthogonal regression method (Akritas & Bershady 1996) on the logarithm of luminosity and temperature, we found as the best-fitting linear relation

$$\log\left(\frac{L_{\text{bol}}(r_{500})}{h(z)}\right) = A_{LT} + B_{LT} \cdot \log\left(\frac{k_{\text{B}}T}{5}\right), \quad (4)$$

with the intercept  $A_{LT} = 44.33 \pm 0.1$ , the slope  $B_{LT} = 3.3 \pm 0.6$ , and the Hubble parameter  $h(z)$  (compare right panel of Fig. 10).

Slope and intercept of the  $L - T$  relation are in good agreement with Takey et al. (2013). Larger cluster statistics enabled Takey et al. (2013) to analyse three redshift bins of their sample. Although our slope indeed matches the value derived for their highest redshift bin ( $0.5 \leq z \leq 0.7$ ) best, it does not contradict their intermediate bin ( $0.25 < z < 0.5$ ) either, taking into account the uncertainties of the fits. We restricted the data from their work to  $L_{\text{bol}}h(z)^{-1} > 10^{43} \text{ erg s}^{-1}$ , rendering the lowest luminosity of the sample of Takey et al. (2013) at similar values as our high-redshift sample. The slopes and intercepts were again derived using the BCES method, as described above. The derived fitting parameters are displayed in Fig. 10 with the refitted sample of Takey et al. (2013) in panels a, b, and c for the lowest, medium, and highest of their redshift bins. In panel d we plot the data from our current sample, which only consists of clusters with  $z > 0.75$  from either LBT/MODS spectroscopy or spectra from the literature, as black dots. We generated a combined sample, including the data from Takey et al. (2013) and our high-redshift sample of confirmed clusters in this work, and applied the  $L_{\text{bol}}h(z)^{-1} > 10^{43} \text{ erg s}^{-1}$  cut. The best-fitting parameters for this new sample are  $A_{LT} = 44.535 \pm 0.083$  and  $B_{LT} = 3.45 \pm 0.29$ , the solution is plotted in Fig. 10 as a dashed blue line. It is apparent that using the cut in bolometric luminosity, the parameters of the  $L - T$  relation are in agreement across all analysed redshift bins. Hence, we see no evolution in the  $L - T$  relation with redshifts using the present cluster statistics.

Additionally, we analysed the intrinsic scatter of the data with respect to the derived best-fitting  $L - T$  relation for each sample using the procedure described by Pratt et al. (2009). We first computed the raw scatter of our data points as the error-weighted orthogonal distances to the regression line. The quadratic difference between the raw scatter and the statistical uncertainties now give the intrinsic scatter,  $\sigma_{\log L_{\text{bol}}}$ , of our samples.

We summarize the fitting parameters for the different samples in Table 4.

## 7. Conclusions

In the input sample of 19 extended X-ray sources with empty SDSS fields, we found 13 distant clusters of galaxies with redshifts in the range  $z = 0.75 - 1.27$ . While 6 of these clusters are

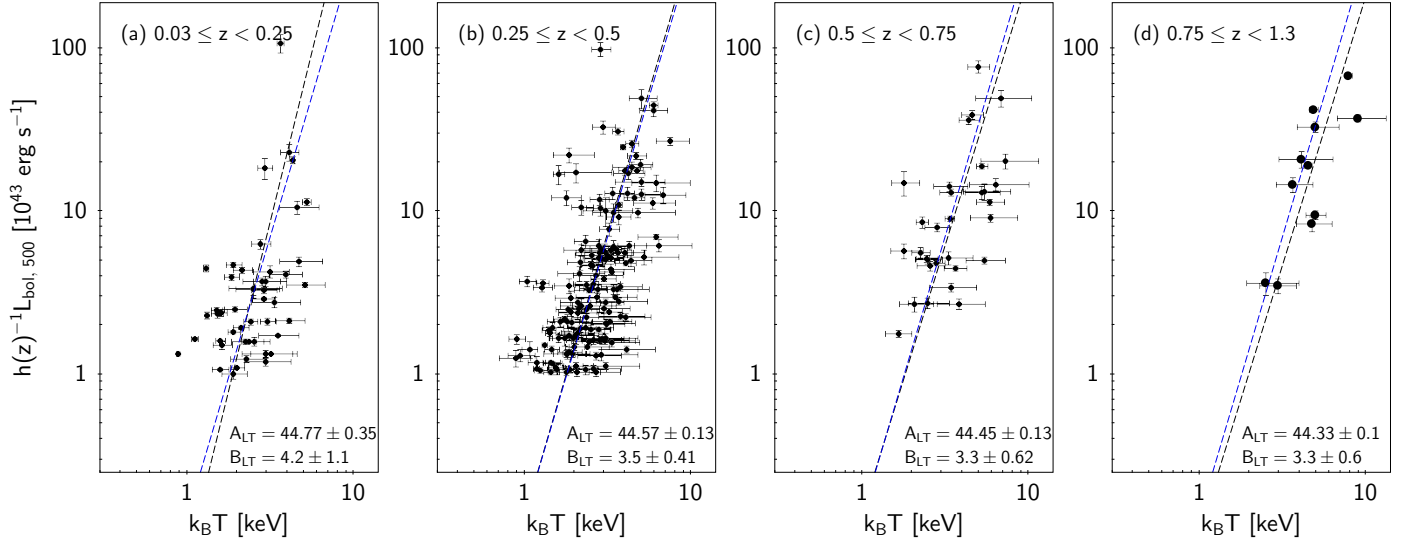


**Fig. 10.** Cluster temperature plotted against the bolometric luminosity of two samples of galaxy clusters. *Panels a–c* show data from [Takey et al. \(2013\)](#), restricted to  $L_{\text{bol}}h(z)^{-1} > 10^{43} \text{ erg s}^{-1}$ , and present their three redshift bins (see individual panel). The clusters from this work are plotted in *panel d*. In all panels we highlight the best-fitting solution of Eq. (6) for the combined sample of [Takey et al. \(2013\)](#) and our high-redshift extension, including the luminosity cut, as a blue dashed line (parameters are listed in Table 4).

**Table 4.** Best-fitting parameters of  $L - T$  relation from the BCES method.

Sample	$n$	Redshift range	$B_{LT}$	$A_{LT}$	$\sigma_{\log L_{\text{bol}}}$
<a href="#">Takey et al. (2013)</a>	47	$0.03 \leq z < 0.25$	$4.2 \pm 1.1$	$44.77 \pm 0.77$	$1.05 \pm 0.15$
<a href="#">Takey et al. (2013)</a>	157	$0.25 \leq z < 0.5$	$3.5 \pm 0.41$	$44.57 \pm 0.13$	$0.543 \pm 0.043$
<a href="#">Takey et al. (2013)</a>	31	$0.5 \leq z < 0.75$	$3.3 \pm 0.62$	$44.45 \pm 0.13$	$0.406 \pm 0.073$
current work	11	$0.75 \leq z < 1.27$	$3.3 \pm 0.6$	$44.33 \pm 0.1$	$0.232 \pm 0.07$
combined	244	$0.03 \leq z < 1.27$	$3.45 \pm 0.29$	$44.535 \pm 0.083$	$0.676 \pm 0.043$

**Notes.** Summary of the BCES fit on the sample with  $L_{\text{bol}}h(z)^{-1} > 10^{43} \text{ erg s}^{-1}$ . The first three columns give the origin of the data, their sample size, and the redshift range of the particular clusters. The resulting best-fitting values for slope and intersect of Eq. (6), their respective errors, and the intrinsic scatter are given in the last three column.

(X-ray selected) objects with identifications and spectroscopic redshifts that have previously been published in the literature, we identified 6 new clusters, measured their redshifts, and also detected a group of four galaxies at the redshift of  $z \sim 1.21$ , using the LBT. The high fraction of confirmed high-redshift clusters demonstrates the efficiency of this selection method, which is based solely on public archival data, for the discovery of these cosmologically interesting objects. The high-redshift objects complement the samples published by [Takey et al. \(2013\)](#), which comprise extended 2XMM sources that have been confirmed as galaxy clusters using SDSS imaging and spectra.

Our spectroscopic LBT observations confirmed the redshift ( $z = 0.99$ ) of the cluster 2XMMp 083026.2+524133, which was previously determined from its X-ray spectrum ([Lamer et al. 2008](#)). The analysis of new *XMM-Newton* observations of this object also confirmed its high X-ray temperature ( $k_{\text{B}}T = 7.82^{+0.4}_{-0.39} \text{ keV}$ ) and luminosity ( $L_{\text{bol}}(r_{500}) = (1168 \pm 4) \times 10^{42} \text{ erg s}^{-1}$ ). However, this cluster optically appears surprisingly inconspicuous, and only eight of the galaxies targeted spectroscopically were found to be cluster members. The resulting constraints to its dynamical mass ( $M_{200} = 5.1^{+6.7}_{-2.9} \times 10^{14} M_{\odot}$ ) are not accurate enough to favour either the high-mass estimates based on the X-ray temperature ( $M_{500} = 5.6 \times 10^{14} M_{\odot}$ ; [Lamer et al. 2008](#)) or the lower estimates from SZ measurements ( $M_{200} = 3.6 \times 10^{14} M_{\odot}/4.7 \times 10^{14} M_{\odot}$ , depending on the model; [Schammell et al. 2013](#)).

We were able to determine meaningful X-ray temperatures and bolometric luminosities for 11 clusters in the new sample. The sample shows a tight  $L - T$  relation of the form

$$\log\left(\frac{L_{\text{bol}}(r_{500})}{h(z)}\right) = (44.33 \pm 0.1) + (3.3 \pm 0.6) \log\left(\frac{k_{\text{B}}T}{5}\right). \quad (5)$$

We have re-analysed the  $L - T$  relation in the sample of [Takey et al. \(2013\)](#) using only clusters with  $L_{\text{bol}}(r_{500})h(z)^{-1} > 10^{43} \text{ erg s}^{-1}$  and find that the  $L - T$  relation in our high-redshift sample and the  $L - T$  relations in all redshift bins of the sample of [Takey et al. \(2013\)](#) are consistent with each other. When we combine our sample with the sample of [Takey et al. \(2013\)](#), the best-fitting  $L - T$  relation is

$$\log\left(\frac{L_{\text{bol}}(r_{500})}{h(z)}\right) = (44.54 \pm 0.1) + (3.45 \pm 0.29) \log\left(\frac{k_{\text{B}}T}{5}\right). \quad (6)$$

When it is compared with the BCES fit to the XMM XXL data ([Giles et al. 2016](#)) without bias correction, the slope for our combined 2XMM sample is somewhat steeper, but still consistent within the errors. It is worth noting that with an intrinsic scatter of  $\sigma_{\log L_{\text{bol}}} = 0.232 \pm 0.07$ , the  $L - T$  relation in the high- $z$  sample is significantly tighter than those of the [Takey et al. \(2013\)](#) and XMM XXL samples. The low scatter might be an indication of a lower fraction of cool-core clusters in the high- $z$  sample. A decline of the cool-core fraction at high redshifts can be expected because of the cosmological evolution of clusters. On the

other hand, at increasing distance, cool-core clusters might also become too compact to be detected as extended X-ray sources.

Finally, we note that for 5 of the 12 clusters we measured X-ray fluxes  $F_{0.5-2}$  above  $3 \times 10^{-14}$  erg cm $^{-2}$  s $^{-1}$ , which is the approximate limit for the detection of extended sources in the eROSITA all-sky survey (Merloni et al. 2012). Given the solid angle of 60 deg $^2$  covered by our survey, we expect several thousand clusters with redshifts  $z > 0.8$  to be discovered by eROSITA.

*Acknowledgements.* We thank the anonymous referee for the constructive report that helped us to improve the readability of the paper. The author acknowledges the use of the TOPCAT<sup>3</sup> and STILTS<sup>4</sup> software packages written by Mark Taylor (2005, 2006). This paper uses data taken with the MODS spectrographs built with funding from NFS grant AST-9987045 and the NSF Telescope System Instrumentation Program (TSIP), with additional funds from the Ohio Board of Regents and the Ohio State University Office of Research. We acknowledge financial support from the ARCHES project (7th Framework of the European Union, No. 313146). Funding for the SDSS and SDSS-II has been provided by the Alfred P. Sloan Foundation, the Participating Institutions, the National Science Foundation, the US Department of Energy, the National Aeronautics and Space Administration, the Japanese Monbukagakusho, the Max Planck Society, and the Higher Education Funding Council for England. The SDSS Web Site is <http://www.sdss.org/>. The SDSS is managed by the Astrophysical Research Consortium for the Participating Institutions. The Participating Institutions are the American Museum of Natural History, Astrophysical Institute Potsdam, University of Basel, University of Cambridge, Case Western Reserve University, University of Chicago, Drexel University, Fermilab, the Institute for Advanced Study, the Japan Participation Group, Johns Hopkins University, the Joint Institute for Nuclear Astrophysics, the Kavli Institute for Particle Astrophysics and Cosmology, the Korean Scientist Group, the Chinese Academy of Sciences (LAMOST), Los Alamos National Laboratory, the Max-Planck-Institute for Astronomy (MPIA), the Max-Planck-Institute for Astrophysics (MPA), New Mexico State University, Ohio State University, University of Pittsburgh, University of Portsmouth, Princeton University, the United States Naval Observatory, and the University of Washington. Based on observations obtained with *XMM-Newton*, an ESA science mission with instruments and contributions directly funded by ESA Member States and NASA. This research has made use of data obtained from the 3XMM *XMM-Newton* serendipitous source catalogue compiled by the 10 institutes of the *XMM-Newton* Survey Science Centre selected by ESA.

## References

- Adelman-McCarthy, J. K., Agüeros, M. A., Allam, S. S., et al. 2008, *ApJS*, **175**, 297
- Akritas, M. G., & Bershady, M. A. 1996, *ApJ*, **470**, 706
- Arnaud, K. A. 1996, in *Astronomical Data Analysis Software and Systems V*, eds. G. H. Jacoby, & J. Barnes, ASP Conf. Ser., 101, 17
- Arviset, C., Guainazzi, M., Hernandez, J., et al. 2002, ArXiv e-prints [[arXiv:astro-ph/0206412](https://arxiv.org/abs/astro-ph/0206412)]
- Becker, R. H., White, R. L., & Helfand, D. J. 1994, in *Astronomical Data Analysis Software and Systems III*, eds. D. R. Crabtree, R. J. Hanisch, & J. Barnes, ASP Conf. Ser., 61, 165
- Beers, T. C., Flynn, K., & Gebhardt, K. 1990, *AJ*, **100**, 32
- Bertin, E., & Arnouts, S. 1996, *A&AS*, **117**, 393
- Bleem, L. E., Stalder, B., de Haan, T., et al. 2015, *ApJS*, **216**, 27
- Böhringer, H., Schuecker, P., Guzzo, L., et al. 2001, *A&A*, **369**, 826
- Buddendiek, A., Schrabback, T., Greer, C. H., et al. 2015, *MNRAS*, **450**, 4248
- Condon, J. J., Cotton, W. D., Greisen, E. W., et al. 1998, *AJ*, **115**, 1693
- Culverhouse, T. L., Bonamente, M., Bulbul, E., et al. 2010, *ApJ*, **723**, L78
- Erben, T., Schirmer, M., Dietrich, J. P., et al. 2005, *Astron. Nachr.*, **326**, 432
- Faber, S. M., Phillips, A. C., Kibrick, R. I., et al. 2003, in *Instrument Design and Performance for Optical/Infrared Ground-based Telescopes*, eds. M. Iye, & A. F. M. Moorwood, Proc. SPIE, 4841, 1657
- Fassbender, R., Böhringer, H., Nastasi, A., et al. 2011, *New J. Phys.*, **13**, 125014
- Finoguenov, A., Guzzo, L., Hasinger, G., et al. 2007, *ApJS*, **172**, 182
- Garilli, B., Fumana, M., Franzetti, P., et al. 2010, *PASP*, **122**, 827
- Gettings, D. P., Gonzalez, A. H., Stanford, S. A., et al. 2012, *ApJ*, **759**, L23
- Giles, P. A., Maughan, B. J., Pacaud, F., et al. 2016, *A&A*, **592**, A3
- Gladders, M. D., & Yee, H. K. C. 2000, *AJ*, **120**, 2148
- Gladders, M. D., & Yee, H. K. C. 2005, *ApJS*, **157**, 1
- Hartmann, D., & Burton, W. B. 1997, *Atlas of Galactic Neutral Hydrogen* (Cambridge, UK: Cambridge University Press), 243
- Hashimoto, Y., Hasinger, G., Arnaud, M., Rosati, P., & Miyaji, T. 2002, *A&A*, **381**, 841
- Hashimoto, Y., Barcons, X., Böhringer, H., et al. 2004, *A&A*, **417**, 819
- Hashimoto, Y., Henry, J. P., Hasinger, G., Szokoly, G., & Schmidt, M. 2005, *A&A*, **439**, 29
- Hasinger, G., Burg, R., Giacconi, R., et al. 1998, *A&A*, **329**, 482
- Hoefl, M., Lamer, G., Kohnert, J., & Schwöpe, A. 2008, ArXiv e-prints [[arXiv:0809.2265](https://arxiv.org/abs/0809.2265)]
- Horne, K. 1986, *PASP*, **98**, 609
- Hurley-Walker, N., Callingham, J. R., Hancock, P. J., et al. 2017, *MNRAS*, **464**, 1146
- Jee, M. J., White, R. L., Ford, H. C., et al. 2006, *ApJ*, **642**, 720
- Kalberla, P. M. W., Burton, W. B., Hartmann, D., et al. 2005, *A&A*, **440**, 775
- Koester, B. P., McKay, T. A., Annis, J., et al. 2007, *ApJ*, **660**, 221
- Lamer, G., Hoefl, M., Kohnert, J., Schwöpe, A., & Storm, J. 2008, *A&A*, **487**, L33
- Lamer, G., de Hoon, A., Fassbender, R., et al. 2011, in *The X-ray Universe 2011*, eds. J.-U. Ness, & M. Ehle, 238
- Lockman, F. J., Jahoda, K., & McCammon, D. 1986, *ApJ*, **302**, 432
- McDonald, M., Bulbul, E., de Haan, T., et al. 2016, *ApJ*, **826**, 124
- Mei, S., Stanford, S. A., Holden, B. P., et al. 2012, *ApJ*, **754**, 141
- Merloni, A., Predehl, P., Becker, W., et al. 2012, ArXiv e-prints [[arXiv:1209.3114](https://arxiv.org/abs/1209.3114)]
- Munari, E., Biviano, A., Borgani, S., Murante, G., & Fabjan, D. 2013, *MNRAS*, **430**, 2638
- Muzzin, A., Wilson, G., Yee, H. K. C., et al. 2009, *ApJ*, **698**, 1934
- Navarro, J. F., Frenk, C. S., & White, S. D. M. 1997, *ApJ*, **490**, 493
- Pacaud, F., Clerc, N., Giles, P. A., et al. 2016, *A&A*, **592**, A2
- Papovich, C. 2008, *ApJ*, **676**, 206
- Peebles, P. J. E. 1993, *Principles of Physical Cosmology* (Princeton University Press)
- Piffaretti, R., Arnaud, M., Pratt, G. W., Pointecouteau, E., & Melin, J.-B. 2011, *A&A*, **534**, A109
- Pogge, R. W., Atwood, B., Brewer, D. F., et al. 2010, in *SPIE Conf. Ser.*, 7735
- Pratt, G. W., Croston, J. H., Arnaud, M., & Böhringer, H. 2009, *A&A*, **498**, 361
- Rosati, P., Stanford, S. A., Eisenhardt, P. R., et al. 1999, *AJ*, **118**, 76
- Rosen, S. R., Webb, N. A., Watson, M. G., et al. 2016, *A&A*, **590**, A1
- Rykoff, E. S., Rozo, E., Hollowood, D., et al. 2016, *ApJS*, **224**, 1
- Schammel, M. P., Feroz, F., Grainge, K. J. B., et al. 2013, *MNRAS*, **431**, 900
- Schirmer, M. 2013, *ApJS*, **209**, 21
- Smith, R. K., Brickhouse, N. S., Liedahl, D. A., & Raymond, J. C. 2001, *ApJ*, **556**, L91
- Stanford, S. A., Elston, R., Eisenhardt, P. R., et al. 1997, *AJ*, **114**, 2232
- Stanford, S. A., Holden, B., Rosati, P., et al. 2001, *ApJ*, **552**, 504
- Sunyaev, R. A., & Zeldovich, Y. B. 1972, *Comments on Astrophysics and Space Physics*, **4**, 173
- Takey, A., Schwöpe, A., & Lamer, G. 2011, *A&A*, **534**, A120
- Takey, A., Schwöpe, A., & Lamer, G. 2013, *A&A*, **558**, A75
- Takey, A., Schwöpe, A., & Lamer, G. 2014, *A&A*, **564**, A54
- Takey, A., Durret, F., Mahmoud, E., & Ali, G. B. 2016, *A&A*, **594**, A32
- Taylor, M. B. 2005, in *Astronomical Data Analysis Software and Systems XIV*, eds. P. Shopbell, M. Britton, & R. Ebert, ASP Conf. Ser., 347, 29
- Taylor, M. B. 2006, in *Astronomical Data Analysis Software and Systems XV*, eds. C. Gabriel, C. Arviset, D. Ponz, & S. Enrique, ASP Conf. Ser., 351, 666
- Thompson, D., Pozzetti, L., Hasinger, G., et al. 2001, *A&A*, **377**, 778
- Šuhada, R., Fassbender, R., Nastasi, A., et al. 2011, *A&A*, **530**, A110
- Vale, C., & White, M. 2006, *New Astron.*, **11**, 207
- Verner, D. A., Ferland, G. J., Korista, K. T., & Yakovlev, D. G. 1996, *ApJ*, **465**, 487
- Voges, W., Aschenbach, B., Boller, T., et al. 1999, *A&A*, **349**, 389
- Watson, M. G., Schröder, A. C., Fyfe, D., et al. 2009, *A&A*, **493**, 339
- Webb, T. M. A., Muzzin, A., Noble, A., et al. 2015, *ApJ*, **814**, 96
- Wilms, J., Allen, A., & McCray, R. 2000, *ApJ*, **542**, 914
- Wilson, G., Muzzin, A., Yee, H. K. C., et al. 2009, *ApJ*, **698**, 1943
- Wright, E. L., Eisenhardt, P. R. M., Mainzer, A. K., et al. 2010, *AJ*, **140**, 1868

<sup>3</sup> <http://www.starlink.ac.uk/topcat/>

<sup>4</sup> <http://www.starlink.ac.uk/stilts/>

## Appendix A: Optical properties from the objects of the LBT/MODS spectroscopic data

**Table A.1.** Properties from optical LBT photometry and spectroscopy for the fields of the six confirmed clusters (Sects. 6.3.1–6.3.6) and the group of galaxies at  $z \sim 1.21$  (Sect. 6.5.1).

Ra	Dec	Redshift	Dist	$r - z$	$z$
2XMMp J083026.2+524133:					
08:30:08	+52:43:32	0.85074	202.2	2.274	20.697
08:30:09	+52:38:50	0.82554	224.5	2.359	21.884
08:30:10	+52:39:12	0.99308*	204.4	2.262	21.898
08:30:12	+52:38:35	0.82364	218.3	2.207	20.427
08:30:12	+52:39:18	0.82624	188.9	2.504	21.14
08:30:19	+52:41:24	0.80204	64.3	2.305	20.715
08:30:19	+52:40:08	0.98185*	108.7	2.471	21.39
08:30:19	+52:41:15	0.79534	65.0	2.225	21.845
08:30:20	+52:40:21	0.98844*	92.3	1.559	20.251
08:30:20	+52:42:48	1.26335	91.1	2.81	21.449
08:30:20	+52:41:47	0.79584	55.6	1.781	20.892
08:30:21	+52:39:31	0.99049*	130.5	2.82	22.501
08:30:22	+52:39:48	0.98337*	110.3	2.461	21.984
08:30:22	+52:42:42	0.85394	78.2	2.504	22.6
08:30:23	+52:43:19	1.03724	110.5	2.928	23.219
08:30:24	+52:41:02	0.73394	36.9	2.088	21.684
08:30:24	+52:43:52	0.71104	140.1	1.661	21.142
08:30:25	+52:43:10	0.95956	97.4	2.411	21.653
08:30:25	+52:42:18	0.95036	46.2	2.372	21.411
08:30:26	+52:41:31	0.45913	3.0	0.726	19.526
<b>08:30:26</b>	<b>+52:41:35</b>	<b>0.98806*</b>	<b>2.9</b>	<b>2.295</b>	<b>20.156</b>
08:30:28	+52:40:49	0.97268*	46.5	2.318	22.539
08:30:31	+52:40:34	0.98147*	71.7	2.505	21.788
08:30:36	+52:42:28	0.71134	103.3	2.11	20.312
08:30:43	+52:38:57	1.06815	218.1	2.305	20.334
2XMMp J092120.2+371735:					
09:21:07	+37:18:08	1.33705	158.3	1.83	21.751
09:21:08	+37:16:43	0.89395	151.9	1.187	21.629
09:21:08	+37:18:09	1.06878	148.7	2.004	22.36
09:21:11	+37:17:55	0.5668	110.7	1.283	21.221
09:21:14	+37:17:44	0.74901	69.3	0.988	23.28
09:21:17	+37:18:00	0.70071	49.4	1.175	21.139
09:21:17	+37:15:40	2.66844	122.0	-0.475	22.972
09:21:18	+37:18:14	0.98443	45.8	1.678	22.235
09:21:18	+37:17:45	1.2089 <sup>‡</sup>	23.5	0.795	22.683
09:21:19	+37:17:40	1.2143 <sup>‡</sup>	15.3	1.991	23.23
09:21:20	+37:17:36	1.21258 <sup>‡</sup>	2.1	1.085	22.004
09:21:20	+37:17:35	1.21365 <sup>‡</sup>	0.9	1.768	22.58
09:21:21	+37:17:26	0.99013	16.9	1.738	21.585
09:21:21	+37:17:32	0.83382	8.4	1.467	22.61
09:21:21	+37:17:32	0.9906	8.4	1.467	22.61
09:21:22	+37:17:22	0.98989	20.2	1.082	21.472

**Notes.** Optical properties of the fields with spectroscopic coverage by LBT/MODS, containing all confirmed clusters (Sects. 6.3.1–6.3.6) and the group of galaxies at  $z \sim 1.21$  (Sect. 6.5.1), with their respective fields indicated, listed in order of ascending RA. Columns 1 and 2 give the position of the object (RA and Dec), Col. 3 the spectroscopic redshift, and in Col. 4 we measure the distance to the X-ray centre in arcseconds. Columns 5 and 6 list the colour  $r - z$  and the  $z$ -band magnitude from LBC imaging. All galaxies classified as cluster members are marked by a star next to their redshift, the BCG is additionally printed bold. The magenta galaxies (2XMMp J133853.9+482033, see 6f and Sect. 6.3.6) are indicated by a dagger, and the high-redshift group of galaxies of the field 2XMMp J093437.4+551340 is marked by a double cross.

**Table A.1.** continued.

Ra	Dec	Redshift	Dist	$r - z$	$z$
09:21:24	+37:16:04	0.82394	100.9	2.039	22.637
09:21:25	+37:16:52	0.5959	67.2	1.038	21.829
09:21:26	+37:17:34	1.0217	70.4	0.67	22.563
09:21:28	+37:15:44	1.47516	147.8	0.156	22.997
09:21:30	+37:17:15	0.23948	119.2	0.098	22.59
09:21:30	+37:16:52	1.03323	121.6	-0.092	23.411
09:21:34	+37:16:40	0.9381	170.0	1.08	23.07
2XMM J093437.5+55134:					
09:34:26	+55:15:36	0.51509	149.0	1.192	20.926
09:34:30	+55:15:12	0.51579	111.8	1.136	21.07
09:34:30	+55:12:17	0.56539	104.3	0.755	24.134
09:34:31	+55:15:57	0.77571	148.3	0.899	21.173
09:34:34	+55:14:17	0.82935	47.3	1.306	22.472
09:34:34	+55:14:45	0.83813*	70.0	2.348	23.521
09:34:36	+55:11:39	0.78881	121.1	2.07	19.745
09:34:37	+55:13:35	0.83465*	8.6	1.661	21.721
09:34:37	+55:13:55	0.83897*	15.2	1.991	22.919
<b>09:34:38</b>	<b>+55:13:45</b>	<b>0.83743*</b>	<b>5.8</b>	<b>2.259</b>	<b>19.637</b>
09:34:39	+55:11:20	0.7254	140.4	1.006	20.558
09:34:39	+55:14:31	0.84478*	52.4	2.138	21.478
09:34:40	+55:14:08	0.53419	37.0	1.205	23.783
09:34:40	+55:13:16	0.83935*	31.7	1.958	23.359
09:34:42	+55:11:29	0.79071	137.9	1.594	22.637
09:34:42	+55:12:09	0.83855*	98.2	1.993	22.447
09:34:44	+55:12:36	0.83875*	84.1	2.063	20.078
09:34:44	+55:12:30	0.84112*	88.4	2.007	23.554
09:34:45	+55:13:27	0.53229	66.8	1.109	21.939
09:34:45	+55:11:50	0.83386*	129.5	1.946	21.403
09:34:46	+55:13:05	0.83992*	82.7	2.045	21.236
09:34:49	+55:16:09	0.51739	178.0	1.054	19.827
09:34:51	+55:16:29	0.53299	207.7	1.267	21.299
2XMMp J105319.8+440817:					
10:53:00	+44:09:12	0.61916	221.0	0.759	21.964
10:53:02	+44:10:05	1.54059	220.0	0.424	19.221
10:53:02	+44:09:57	0.37965	219.2	0.415	21.986
10:53:03	+44:08:38	0.36105	179.0	0.637	21.454
10:53:06	+44:08:40	0.53776	150.3	0.499	21.012
10:53:08	+44:07:57	0.71606	123.9	0.83	24.432
10:53:11	+44:07:38	0.52576	105.7	0.554	23.463
10:53:11	+44:08:05	0.95507	96.5	1.084	23.265
10:53:13	+44:08:26	0.89067*	69.1	1.528	22.672
10:53:16	+44:08:38	0.90261*	42.9	1.881	22.929
10:53:17	+44:07:13	0.62226	70.6	0.955	21.537
10:53:18	+44:08:08	0.89934*	17.0	1.677	21.513
<b>10:53:20</b>	<b>+44:08:18</b>	<b>0.89726*</b>	<b>4.0</b>	<b>1.562</b>	<b>20.964</b>
10:53:20	+44:08:06	0.89211*	11.6	1.426	23.087
10:53:21	+44:08:17	3.83538	8.6	0.812	22.346
10:53:22	+44:08:21	0.90092*	21.8	1.728	20.988
10:53:22	+44:08:21	0.89109*	21.8	1.728	20.988
10:53:22	+44:09:25	0.72856	71.0	1.019	21.382
10:53:24	+44:11:21	0.50556	189.0	0.598	20.023
10:53:25	+44:08:27	0.8905*	59.3	1.738	22.64
10:53:26	+44:08:27	0.51166	62.2	0.545	23.228
10:53:26	+44:08:45	0.41305	72.3	0.502	22.868
10:53:27	+44:08:57	0.50836	86.2	0.97	19.547
10:53:27	+44:08:59	0.50586	91.6	0.935	20.177
10:53:28	+44:10:26	0.36455	156.5	0.587	21.83
10:53:29	+44:09:21	0.04474	118.8	0.275	21.06
10:53:29	+44:10:57	0.38405	185.5	0.653	21.342
10:53:35	+44:08:25	0.61996	162.5	1.192	22.189
2XMMp J120815.5+250001:					
12:08:05	+24:57:45	0.73941	197.4	1.739	22.057
12:08:05	+24:57:48	0.99166*	195.0	2.334	20.805

Table A.1. continued.

Ra	Dec	Redshift	Dist	$r - z$	$z$
12:08:09	+24:58:05	0.74001	146.0	1.893	20.18
12:08:10	+25:00:40	1.20921	85.9	2.837	22.764
12:08:11	+25:02:25	2.94232	157.4	0.156	24.134
12:08:11	+25:02:33	0.29081	163.6	0.642	23.147
12:08:12	+24:58:53	0.98141*	82.6	2.476	22.569
12:08:12	+25:01:50	1.09921	116.3	2.242	22.476
12:08:13	+25:02:05	0.96539	128.1	1.579	21.85
<b>12:08:15</b>	<b>+25:00:01</b>	<b>0.99577*</b>	<b>4.9</b>	<b>2.38</b>	<b>20.262</b>
12:08:15	+24:59:04	1.00135*	58.0	2.165	23.102
12:08:16	+25:00:19	1.0042*	18.4	2.376	20.113
12:08:16	+25:02:55	0.99633*	173.7	2.124	21.191
12:08:16	+25:00:23	0.99824*	21.8	2.283	21.511
12:08:17	+24:59:37	0.98198*	28.2	1.983	21.569
12:08:17	+24:59:46	1.006*	30.7	2.415	21.441
12:08:18	+24:59:53	0.98387*	28.3	2.373	20.7
12:08:18	+24:59:56	0.99076*	37.1	2.468	20.72
12:08:18	+24:59:20	1.32411	52.6	1.915	24.613
12:08:18	+24:59:22	0.96715	50.8	2.433	22.395
12:08:18	+25:00:55	0.98487*	65.9	2.024	23.334
12:08:18	+25:01:02	0.9957*	72.2	2.665	22.577
12:08:19	+25:00:09	0.31021	48.3	0.562	22.395
12:08:19	+25:00:47	0.99948*	65.5	2.685	22.974
12:08:20	+24:59:28	0.98472*	65.2	1.986	21.428
12:08:20	+24:58:31	0.96529	112.6	2.231	22.371
12:08:20	+24:57:36	1.19821	157.1	2.074	22.573
12:08:20	+24:58:20	0.9671	121.3	1.859	21.983
12:08:23	+25:01:29	1.20841	130.5	2.662	21.697
12:08:25	+25:03:09	1.20721	225.8	2.534	22.137
12:08:25	+25:01:17	0.98985*	149.7	2.166	22.094

## 2XMMp J123759.3+180332:

12:37:47	+18:01:27	0.70178	215.1	1.908	20.081
12:37:47	+18:02:13	1.03447	186.7	2.252	22.763
12:37:48	+18:05:04	1.03457	184.3	2.576	22.752
12:37:49	+18:01:07	0.54928	207.2	0.915	21.213
12:37:49	+18:01:09	0.50588	205.0	0.56	20.311
12:37:49	+18:03:40	1.03447	141.2	2.181	22.741
12:37:51	+18:01:28	1.08897	173.3	2.505	22.277
12:37:51	+18:03:12	0.89852*	120.3	2.27	21.457
12:37:52	+18:01:43	1.03487	153.8	2.486	22.417
12:37:52	+18:01:59	0.77898	139.1	1.9	22.713
12:37:52	+18:00:49	0.81397	194.1	2.114	22.68
12:37:52	+18:01:09	1.08947	177.5	2.377	22.05
12:37:54	+18:01:29	0.70028	145.8	1.828	20.792
12:37:56	+18:02:30	0.89224*	78.6	2.328	22.279
12:37:57	+18:03:12	0.87744*	43.5	2.038	22.654
12:37:58	+18:02:11	0.88378*	81.7	1.99	21.797
12:37:58	+18:02:59	0.87475*	35.6	1.985	23.184
<b>12:37:59</b>	<b>+18:03:32</b>	<b>0.88625*</b>	<b>1.0</b>	<b>2.176</b>	<b>20.238</b>
12:37:59	+18:03:34	0.89474*	2.2	1.996	21.267
12:37:59	+18:06:25	1.02937	173.0	2.295	21.376
12:37:59	+18:03:27	0.89575*	7.9	2.253	21.536
12:38:00	+18:03:31	0.8908*	6.9	2.346	21.364
12:38:00	+18:03:45	0.889*	14.6	2.25	21.106
12:38:01	+18:03:44	0.89698*	28.2	2.176	21.552
12:38:03	+18:04:05	0.89132*	65.1	2.02	22.315
12:38:03	+18:04:22	0.8842*	71.8	2.253	22.199
12:38:04	+18:04:36	0.88215*	95.8	2.032	22.514
12:38:04	+18:02:58	0.82977	69.4	1.646	23.756
12:38:05	+18:04:37	0.8787*	99.2	2.045	21.844
12:38:05	+18:04:38	0.88015*	100.6	2.132	22.129

## 2XMMp J133853.9+482033:

13:38:43	+48:19:28	1.0354	124.2	2.452	21.25
13:38:44	+48:20:24	1.1375	100.4	2.083	21.294

Table A.1. continued.

Ra	Dec	Redshift	Dist	$r - z$	$z$
13:38:45	+48:19:41	1.0314	101.5	2.092	24.444
13:38:45	+48:19:38	1.029	103.4	1.866	21.007
13:38:45	+48:19:32	1.0294	106.5	2.227	22.328
13:38:48	+48:22:38	0.2558	138.0	-0.201	23.083
13:38:49	+48:19:26	0.7493*	84.0	2.003	21.653
13:38:51	+48:20:02	0.749*	43.1	1.69	21.458
13:38:53	+48:22:20	0.8586	107.2	2.167	21.757
13:38:53	+48:20:28	0.7504*	14.1	2.024	21.159
13:38:54	+48:19:43	0.7558†	50.1	1.844	21.086
13:38:54	+48:20:22	0.7498*	11.1	1.951	20.896
13:38:55	+48:20:30	0.7553†	11.8	1.991	19.506
<b>13:38:55</b>	<b>+48:19:15</b>	<b>0.7501*</b>	<b>77.9</b>	<b>1.59</b>	<b>20.144</b>
13:38:55	+48:23:31	0.7561†	178.6	1.745	20.683
13:38:55	+48:20:39	0.7532†	14.6	1.69	21.597
13:38:56	+48:21:10	0.7507*	41.5	1.318	24.604
13:38:56	+48:21:09	0.862	39.8	1.961	21.557
13:38:57	+48:20:37	0.7485*	33.6	1.691	20.76
13:38:59	+48:19:20	0.7496*	90.2	1.924	22.349
13:39:01	+48:21:57	1.0962	108.6	2.773	22.928
13:39:05	+48:22:43	1.0414	171.9	1.381	22.034
13:39:06	+48:20:52	0.8953	125.4	2.517	21.278

**Appendix B: Clusters with redshifts from the literature and no LBC imaging**

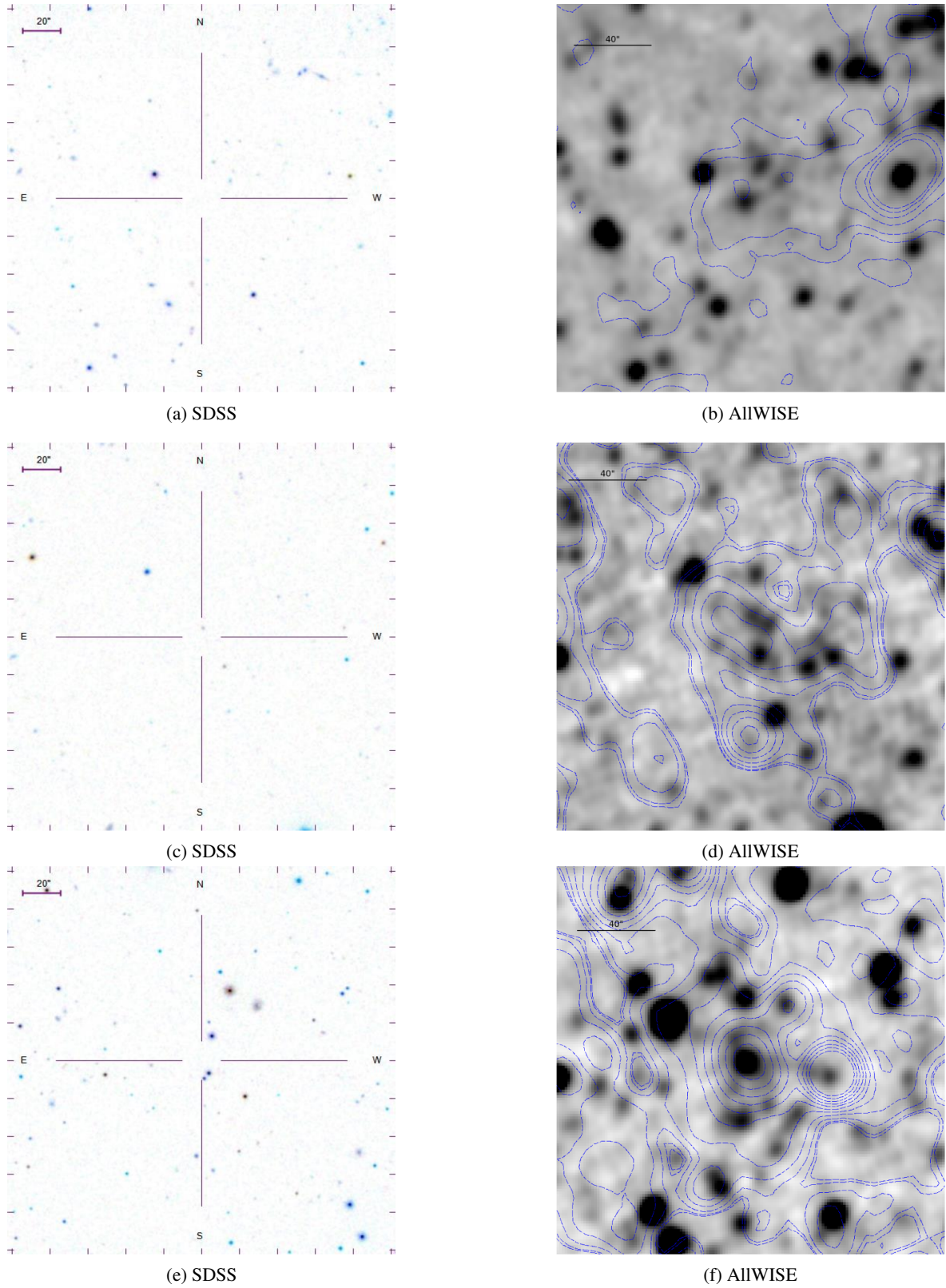


**Fig. B.1.** Optical and near-IR images of the fields 2XMMp J030212.0-000133 (*top panels*), 2XMMp J084836.4+445345 (*middle*), and 2XMMp J084858.3+445158 (*bottom*). North is up, east is left, and both images cover the same region. Figures on the left side show SDSS DR6 images, while W1-band ( $3.4 \mu\text{m}$ ) images from the AllWISE survey are on the right side. Blue dashed lines are the contours from the X-ray emission, but not at the same flux levels.

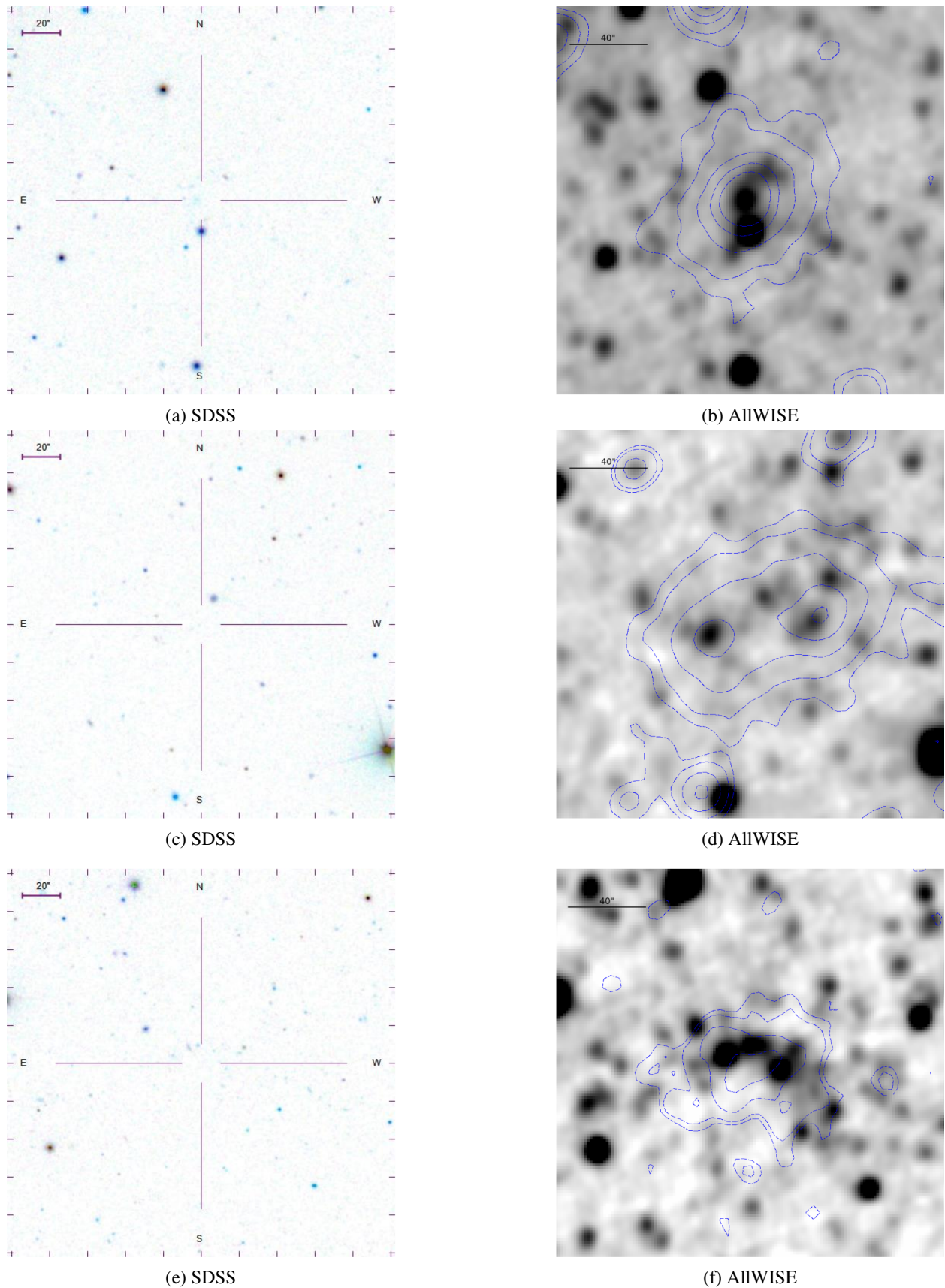
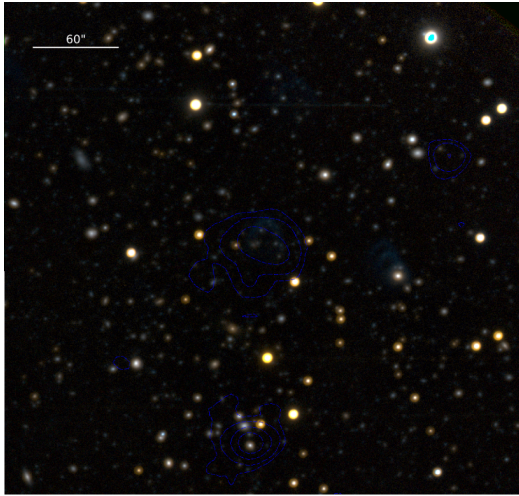
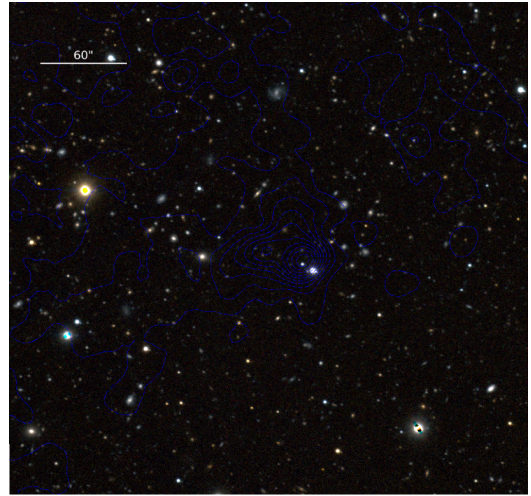


**Fig. B.2.** Optical and near-IR images of the fields 2XMMp J100451.6+411626 (*top panels*), 2XMMp J105344.2+573517 (*middle*), and 2XMMp J123113.1+154550 (*bottom*). North is up, east is left, and both images cover the same region. Figures on the left side show SDSS DR6 images, while W1-band ( $3.4 \mu\text{m}$ ) images from the AllWISE survey are on the right side. Blue dashed lines are the contours from the X-ray emission, but not at the same flux levels.

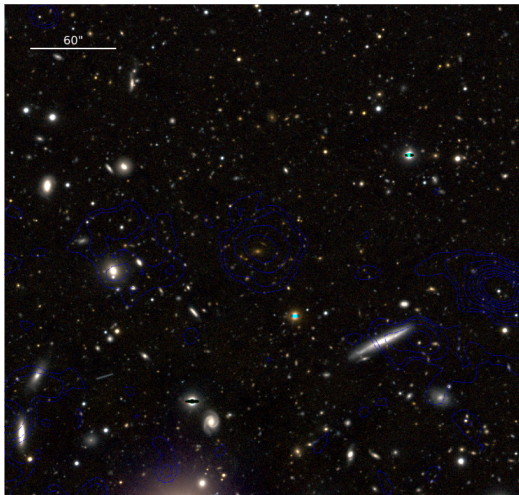
**Appendix C: Rejected and unclassified fields**



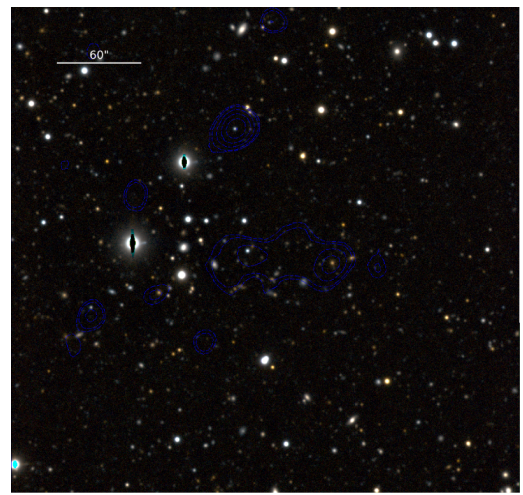
(a) 2XMMp J093607.2+613245



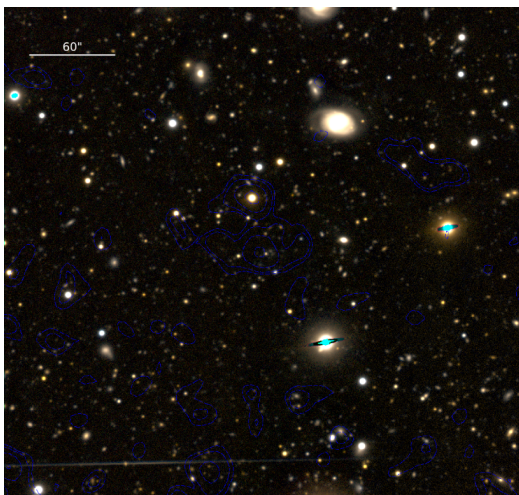
(b) 2XMMp J120735.1+250538



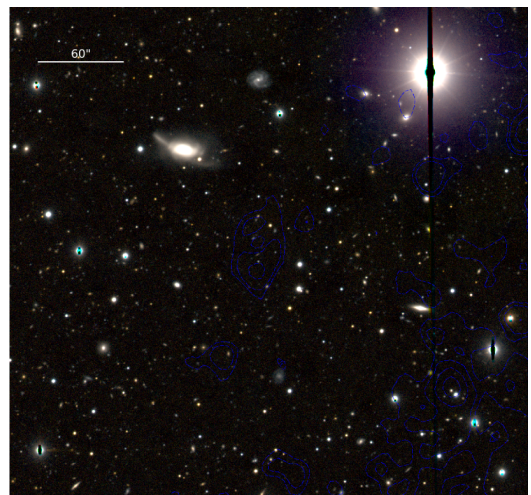
(c) 2XMMp J133038.6-013832



(d) 2XMMp J144854.8+085400



(e) 2XMMp J145220.8+165458



(f) 2XMMp J151716.8+001302

**Fig. C.1.** LBC colour images of the rejected or unclassified fields of Sect. 6.5. We assigned  $r$ -SLOAN and  $z$ -SLOAN images from the LBC to the blue and red channel of the colour image. The green channel was created from the mean of both bands. Blue dashed lines are the contours from the X-ray emission, but not at the same flux levels for all subimages. North is up, east is left, and the images are centred on the respective X-ray position.

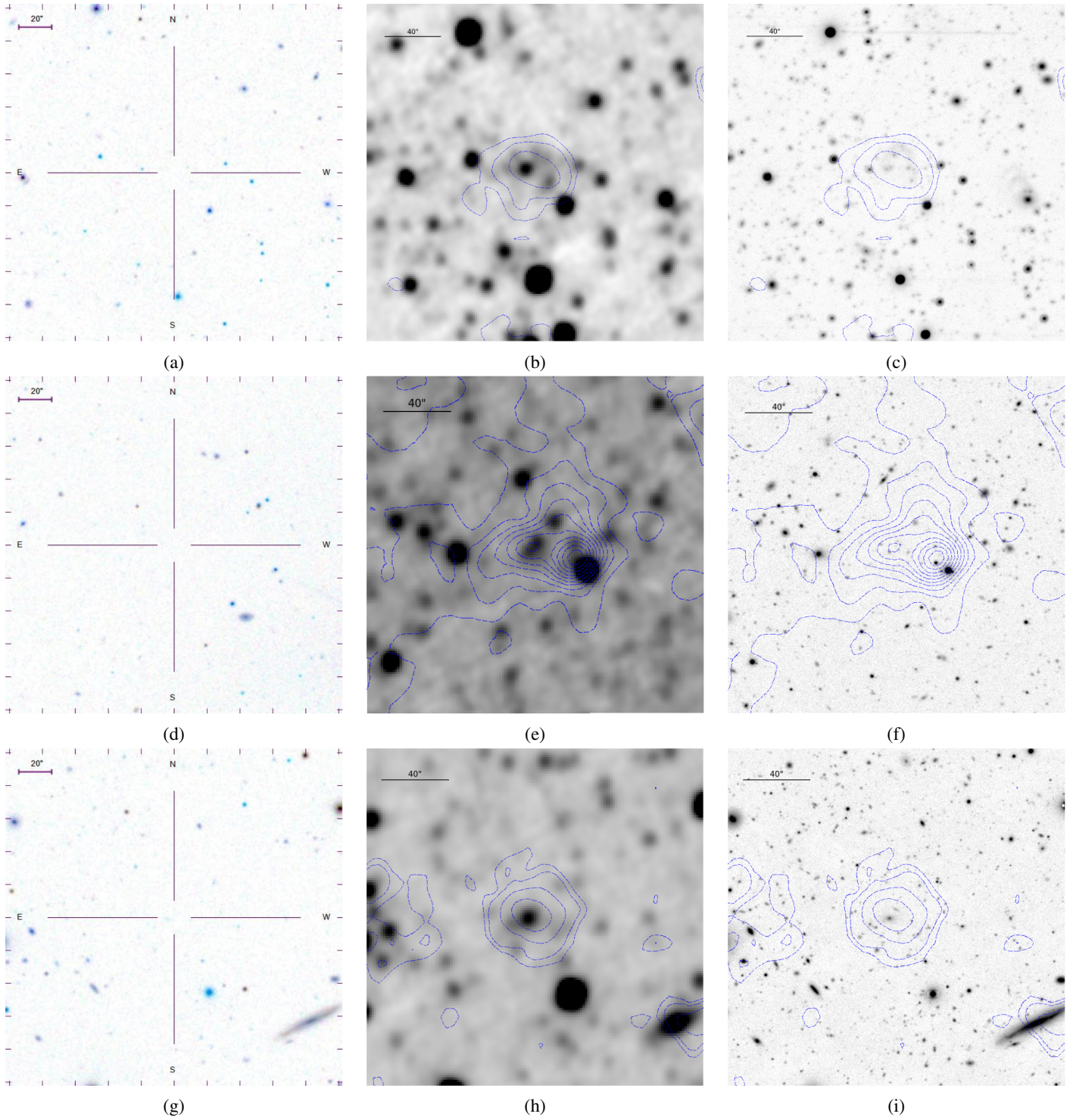


**Fig. C.2.** Optical and near-IR images of the fields of 2XMMp J093607.2+613245 (*top row*), 2XMMp J120735.1+250538 (*middle*), and 2XMMp J133038.6-013832 (*bottom*). The first column shows SDSS cutouts of the respective fields, the central column the W1-band ( $3.4 \mu\text{m}$ ) images from the AllWISE survey, and on the right side, we present LBC images (mean of the  $r$ - and  $z$ -SLOAN filters). Images of each row are centred at the respective X-ray positions and show the same region of the sky. Blue dashed lines (*middle and right images*) indicate contours from the X-ray flux, where the levels are chosen for illustration alone. North is up, east is left, and the images are centred on the respective X-ray position.

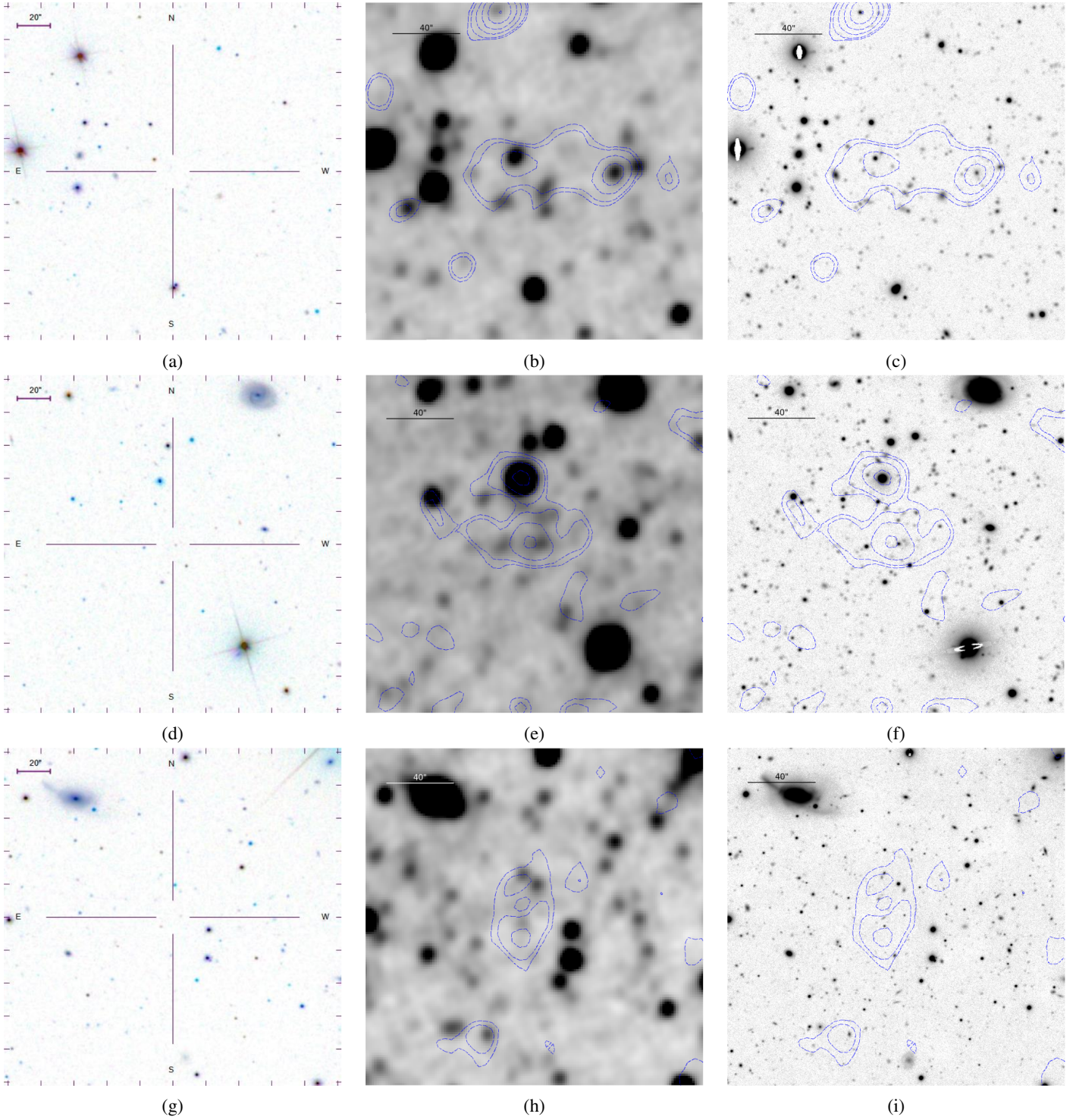


**Fig. C.3.** Optical and near-IR images of the fields of 2XMMp J144854.8+085400 (*top row*), 2XMMp J145220.8+165458 (*middle*), and 2XMMp J151716.8+001302 (*bottom*). The first column shows SDSS cutouts of the respective fields, the central column the W1-band ( $3.4\ \mu\text{m}$ ) images from the AllWISE survey, and on the right side, we present LBC images (mean of the  $r$ - and  $z$ -SLOAN filters). Images of each row are centred at the respective X-ray positions and show the same region of the sky. Blue dashed lines (*middle and right images*) indicate contours from the X-ray flux, where the levels are chosen for illustration alone. North is up, east is left, and the images are centred on the respective X-ray position.

**Appendix D: Properties of archival *XMM-Newton* observations****Table D.1.** X-ray catalogue properties of the selected cluster candidates.

OBSID	2XMMp...	EP_EXTENT [ $''$ ]	3XMM-DR6...	EP_EXTENT [ $''$ ]	M1/M2/PN [ks]
0041170101	J030212.0-000133	$9.3 \pm 1.3$	J030212.1-000132	$8.5 \pm 1.3$	46.7/46.7/37.3
0092800101	J083026.2+524133	$18.4 \pm 1.1$	J083026.2+524133	$18.8 \pm 1.1$	16.3/16.4/12.4
0092800201	J083026.2+524133	$16.48 \pm 0.4$	J083026.2+524133	$16.18 \pm 0.43$	71.9/72.3/62.3
0502220201	–	–	J083026.2+524133	$18.47 \pm 0.57$	56.1/61.4/37.2
0502220301	–	–	J083026.2+524133	$17.64 \pm 0.5$	72.4/73.3/58.4
0085150101	J084836.4+445345	$9.7 \pm 1.9$	J084836.1+445343	$12.6 \pm 2.1$	39.8/39.8/36.4
0085150201	J084836.4+445345	$0.0 \pm 0.0$	J084836.1+445343	$0.0 \pm 0.0$	19.3/19.2/17.9
0085150301	–	–	J084836.1+445343	$0.0 \pm 0.0$	–/–/22.3
0085150101	J084858.3+445158	$12.29 \pm 0.86$	J084858.4+445158	$12.41 \pm 0.9$	39.8/39.8/36.4
0085150201	J084858.3+445158	$13.9 \pm 1.2$	J084858.4+445158	$10.15 \pm 0.95$	19.3/19.2/17.9
0085150301	J084858.3+445158	$8.7 \pm 1.3$	J084858.4+445158	$10.3 \pm 1.4$	–/–/22.3
0149010201	J092120.2+371735	$11.6 \pm 1.6$	J092120.2+371735	$13.1 \pm 1.8$	54.2/54.3/46.4
0112520101	J093437.4+551340	$8.4 \pm 1.2$	J093437.5+551342	$8.30 \pm 1.3$	28.5/28.3/22.4
0112520201	–	–	J093437.5+551342	$9.4 \pm 2.1$	10.4/10.4/9.8
0085640201	J093607.2+613245	$9.98 \pm 0.69$	J093607.3+613245	$9.28 \pm 0.69$	
0207130201	J100451.6+411626	$6.65 \pm 0.24$	J100451.6+411627	$6.45 \pm 0.28$	33.5/33.5/30.2
0146990201	–	–	J105320.2+440815	$14.9 \pm 2.4$	11/10.9/6.9
0146990901	J105319.8+440817	$13.6 \pm 2.3$	J105320.2+440815	$14.6 \pm 2.7$	5.1/5.5/4
0022740201	J105344.2+573517	$33.9 \pm 2.6$	J105343.5+573518	$26.2 \pm 1.50$	26.7/26.7/23.8
0123700101	J105344.2+573517	$23.8 \pm 1.9$	J105343.5+573518	$30.3 \pm 2.1$	32.8/32.8/29.9
0123700401	–	–	J105343.5+573518	$33.1 \pm 3.2$	12.2/12.4/11.9
0147510901	J105344.2+573517	$28.2 \pm 1.4$	J105343.5+573518	$27.4 \pm 1.4$	40.6/40.5/37.8
0147511101	J105344.2+573517	$27.2 \pm 1.2$	–	–	24.5/24.5/22.7
0147511301	J105344.2+573517	$32 \pm 1.9$	J105343.5+573518	$38.6 \pm 2.2$	15/15/13.9
0147511601	J105344.2+573517	$23.2 \pm 1.1$	J105343.5+573518	$25.9 \pm 1$	98.1/98.4/89.4
0147511701	–	–	J105343.5+573518	$24.5 \pm 1.1$	89.8/89.9/81.7
0147511801	J105344.2+573517	$29.8 \pm 1.2$	J105343.5+573518	$29 \pm 1.1$	65.4/65.5/60.2
0151400201	J120735.1+250538	$6.6 \pm 1.3$	J120735.2+250537	$7.8 \pm 1.5$	13/13.2/9.4
0151400201	J120815.5+250001	$24.2 \pm 3.2$	J120816.0+250002	$20.8 \pm 2.7$	13/13.2/9.4
0106061001	J123113.1+1545508	$20.9 \pm 1.7$	J123113.1+154548	$19.5 \pm 1.6$	5.6/5.6/5
0200020101	J123759.3+180332	$13 \pm 1.3$	J123759.2+180335	$14.4 \pm 1.4$	13.3/13.5/9.7
0112240301	J133038.6-013832	$6.8 \pm 1$	J133038.7-013832	$6.82 \pm 0.92$	
0152940101	J133852.5+044309	$15.7 \pm 1.9$	J133852.4+044309	$23.2 \pm 2.3$	
0055990501	J133853.9+482033	$7.6 \pm 1.3$	J133854.1+482034	$6.8 \pm 1.2$	18/18.1/13
0057560301	J144854.8+085400	$15.6 \pm 1.5$	J144854.7+085359	$16.6 \pm 1.6$	
0148520101	–	–	J144854.7+085359	$15.3 \pm 2.3$	
0148520301	J144854.8+085400	$29.9 \pm 3.6$	J144854.7+085359	$28.5 \pm 3.5$	
0091140201	J145220.8+165458	$6.2 \pm 1.2$	J145220.6+165457	$0.0 \pm 0.0$	
0103860601	J151716.8+001302	$7.6 \pm 1.8$	J151716.9+001258	$8 \pm 1.8$	
0201902001	–	–	J151716.9+001258	$0.0 \pm 0.0$	

**Notes.** The OBSIDs for the individual cluster candidates selected in this work are listed in Col. 1. We identify the corresponding X-ray source in the 2XMMp catalogue in Col. 2 and list its extent measured from the respective OBSID in Col. 3. Columns 4 and 5 add the same properties for the 3XMM-DR6 catalogue. We note again that 2XMMp was decisive for the selection of the sample, while the X-ray analysis further included more recent *XMM-Newton* observations. Differences in source position and extent between the two catalogues can be addressed to updates in their respective reduction procedures. The last column lists the available cleaned exposure time per EPIC instrument for the confirmed clusters, either in this or other works.